frontiers | Frontiers in Marine Science

ORIGINAL RESEARCH
published: 01 April 2022
doi: 10.3389/fmars.2022.612021

Submarine Geomorphology and Glacimarine Sedimentary Processes Associated to Deglaciation in Europa Fjord, Chilean Patagonia

Cristián Rodrigo[1], Erick Cifuentes[2], Rodrigo Fernández[3], José Andrade[1], Lorena Rebolledo[4,5], Diego Muñoz[6] and Práxedes Muñoz[7,8]*

[1] Geologia, Facultad de Ingenieria, Universidad Andres Bello, Viña del Mar, Chile, [2] Departamento de Ciencias de la Tierra, Facultad de Quimica, Universidad de Concepción, Concepción, Chile, [3] Departamento de Geologia, Facultad de Ciencias Fisicas y Matematicas, Universidad de Chile, Santiago, Chile, [4] Departamento Cientifico, Instituto Antartico Chileno, Punta Arenas, Chile, [5] Centro de Investigacion Dinamica de Ecosistemas Marinos de Altas Latitudes (IDEAL), Punta Arenas, Chile, [6] Departamento de Hidrografia, Servicio Hidrografico y Oceanografico de la Armada, Valparaíso, Chile, [7] Departamento de Biología Marina, Universidad Católica del Norte, Coquimbo, Chile, [8] Centro de Estudios Avanzados en Zonas Áridas (CEAZA), La Serena, Chile

OPEN ACCESS

Edited by:
Giorgio Bavestrello, University of Genoa, Italy

Reviewed by:
Min Kyung Lee, Korea Polar Research Institute, South Korea
Giovanni Daneri, Patagonian Ecosystems Investigation Research Center (CIEP), Chile

****Correspondence:***
Cristián Rodrigo
cristian.rodrigo@unab.cl

Specialty section:
This article was submitted to Marine Biogeochemistry, a section of the journal Frontiers in Marine Science

Received: *16 November 2020*
Accepted: *25 February 2022*
Published: *01 April 2022*

Citation:
Rodrigo C, Cifuentes E, Fernández R, Andrade J, Rebolledo L, Muñoz D and Muñoz P (2022) Submarine Geomorphology and Glacimarine Sedimentary Processes Associated to Deglaciation in Europa Fjord, Chilean Patagonia. Front. Mar. Sci. 9:612021. doi: 10.3389/fmars.2022.612021

In a period of high rates of glacier retreat, increasing meltwater discharge from tidewater glaciers can influence marine fjord ecosystems due to increase sediment delivery and accumulation rates in the proglacial environment. Glacier variations and associated changes in glacimarine processes are recorded in the sedimentary record and submarine geomorphology of fjords. In October-November 2017, CIMAR23 Cruise surveyed several fjords adjacent to the Southern Patagonian Icefield (SPI). In this study, we show detailed results of the multibeam bathymetry, backscatter and sub-bottom seismic profiles, and sediment core samples from Europa Fjord, located west of the central SPI area, to improve the analysis of the fjord glacial and sedimentary evolution and to connect its behavior with the other fjords in the region. For the cores ^{210}Pb chronology, magnetic susceptibility, organic carbon, total nitrogen, and stable isotopes ($\delta^{13}C_{org}$, $\delta^{15}N$) were performed. The seafloor geomorphology showed that the most prominent submarine landforms are transverse morainal ridges, which indicate past stillstand glacier positions; these features formed during the deglaciation of the fjord (latest Pleistocene), and some, perhaps more recently during short episodic advance/retreat events. In the central and mouth fjord areas, erosional features such as lineations are found on the rocky bottom and interpreted as formed by past grounded glaciers. Several submarine moraines are generally well preserved, but some parts are crumbled by slope failures and erosion. Most of the seismic sections are interpreted as the expected subglacial-ice proximal-ice distal succession of facies, characteristic of single retreat environments. The sedimentary record includes bioturbed muds with muddy laminations and variable amounts of coarse sediments interpreted as ice rafted debris, suggesting a proglacial environment, punctuated by calving. From the beginning of the twentieth century there is a tendency to an increase in the terrigenous organic

material content, including an abrupt increase during the 80–90s, and a decline in the last decade. This behavior is indicating possibly a general increase of surface terrestrial runoff and, for the last decade, an increase of glacial meltwater input which would be caused by an accelerated deglaciation.

Keywords: acoustic data, seafloor, submarine landforms, sediments, tidewater glacier, fjord, climate change, Patagonia

INTRODUCTION

The sea floor geomorphology and glacimarine sedimentary processes of the fjords of western Patagonia are the result of a long history of glacial influence in the region. The last fully glacial conditions occurred associated with the Late Pleistocene Patagonian Ice Sheet (LPPIS), which was a large ice body that extended along the Southern Andes, between 30 and 56°S. The LPPIS covered ∼492,600 km^2 during glacial maxima conditions about 33–28 ka (Davies et al., 2020), which equals to more than 25 times the present-day glaciated area. After 18 ka, the relatively rapid shrinking of the LPPIS allowed the initiation of sedimentary glacimarine processes in the western fjords and the continental shelf of Patagonia. The LPPIS was separated in two ice bodies north and south of Canal Martinez-Baker at ∼13 ka (Turner et al., 2005); further shrinking of these ice masses would constitute the present-day Northern Patagonian Icefield (NPI) (46°35′S–47°35′S), and the Southern Patagonian Icefield (SPI) (48°20′S–51°30′S).

After the deglaciation of the Patagonian fjords, the Holocene extent of Patagonian glaciers, varied in a manner characterized by termini advance and retreat within at most, a few 10s of kilometers of the fjords' head, although studied areas are scarce and few (e.g., Harrison, 2004; Koppes et al., 2015). Available chronological and geomorphological data indicate that most SPI glaciers were near their maximum Late Holocene glacier extent state between the sixteenth and nineteenth centuries (Masiokas et al., 2009; Glasser et al., 2011), period that was followed by widespread glacier shrinkage during the twentieth century (Rivera et al., 2012). The twentieth century glacier retreat has been explained by regional increase in temperatures accompanied by decreasing precipitation, possibly associated to global climate changes resulting from the anthropogenic emission of greenhouse gases (Carrasco et al., 1998; Rignot et al., 2003; Gardner et al., 2013; IPCC, 2014; Marzeion et al., 2014). The shrinkage of SPI and increasing production of meltwater accounts for about 9% of the contribution from global mountain glaciers to the rate of sea level rise (Rignot et al., 2003), which highlights its importance for the present-day changing Earth System. Changes in sediment discharge associated with meltwater production, influence the biogeochemical cycles and ecosystems of fjords (e.g., Iriarte et al., 2010; Quiroga et al., 2013; Seifert et al., 2019), especially those most directly related to the seafloor such as benthic organisms (e.g., Quiroga et al., 2016). These environmental changes, includings changes in marine productivity, and geochemical characteristics, can be recorded in the fjord sediments, allowing the study of patterns of oceanographic and biological variables and their evolution (e.g., Rebolledo et al., 2008, 2011, 2019; Aracena et al., 2011; Silva et al., 2011).

The majority of SPI outlet glaciers are either fjord-calving tidewater glaciers or lake-calving glaciers, whose glacial and sedimentary dynamics are complex, especially in changing climate scenario (Moon et al., 2012; Schenk and Csatho, 2012). Numerous studies suggest that while climate may trigger changes in tidewater glacier mass balance and extent, the rate of retreat is mainly controlled by the unique geometry, shape, width and bathymetry of its channeling fjord, while stillstands and advance episodes are likely controlled by the capacity of construction of stabilizing grounding line moraines (Pfeffer, 2007; Briner et al., 2009; Post et al., 2011; Enderlin and Howat, 2013). In recent years, important steps forward to understand glacier behavior have been made in Patagonia (e.g., Koppes et al., 2009; Rivera et al., 2012), however, most of the studies focus on just a few case-study calving glaciers and are descriptive of recent changes, providing little information about the glacial and sedimentary processes at work and their influence on the glacimarine environment; nevertheless several studies demonstrate that the marine sedimentary record from the proglacial glacimarine environment can preserve a record of the spatial-temporal interactions between the glacier behavior, and climate and ocean changes (e.g., Boyd et al., 2008; Koppes et al., 2009, 2015; Fernández et al., 2012, 2017; Bertrand et al., 2017). On the other hand, the identification of submarine glacial morphologies has led to a better understanding of sub-glacial and proglacial processes and advance and retreat cycles (e.g., Rivera et al., 2012; Dowdeswell and Vásquez, 2013; Dowdeswell et al., 2016). In this work we present results from a marine geology study aimed at characterizing the recent and modern environmental and sedimentary conditions at Europa Fjord a 58 km long fjord located west of the central SPI area (∼50°10′S; **Figure 1**), that has the only one calving glacier, Europa Glacier, which is located at the fjord head. Like the majority of the SPI glaciers, Europa glacier has retreated over the last decades; however, relative to other SPI glaciers, its retreat rate is rather slow, not exceeding 300 m between 1984 and 2011 (Sakakibara and Sugiyama, 2014). Another particularity of Europa Glacier is that exhibits erosion rates of ∼0.14 mm yr^{-1} at millennial timescales, much lower than other Patagonian glaciers, and comparable to subpolar Antarctic sites (Fernández et al., 2016), which in principle, signify that it has a relatively low sediment production. Considering these particularities and the location of the Europa fjord in the SPI region, in this work we present detailed results on submarine geomorphology, seismic stratigraphy and characteristics of surface sedimentology, to specify the phenomena associated with glacial evolution and sedimentary processes of the Europa fjord, identifying its

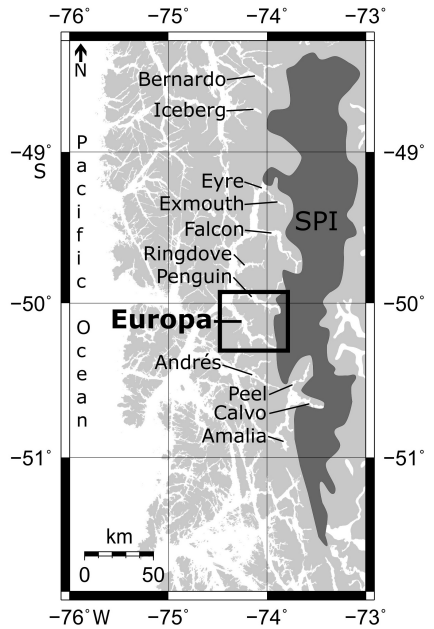

FIGURE 1 | Study area and Europa Fjord location. Approximate Southern Patagonian Icefield (SPI) coverage in the present time. Main fjords of the region are also identified.

behavior and providing background information to establish its connection with other fjords in the region, in order to contribute to a better understanding of the sensitive contact zone between glaciers and the marine environment.

MATERIALS AND METHODS

Study Area

The study area is in the Magallanes Region, Chilean Patagonia, between latitudes 49.95 and 50.33°S and longitudes 74.50 and 73.75°W (**Figure 1**), in which is located the Europa Fjord and its same name tidewater glacier, corresponding to an outlet glacier from the SPI, in the area of the Bernardo O'Higgins National Park.

The fjord has a length of ∼58 km, a maximum width of ∼6 km in its mouth, and a minimum width of 1 km in its head. It is oriented NW-SE and it is sinuous in its medial and proximal part with respect to the glacier front. Deeper areas are close to the fjord mouth (∼780 m) and the shallower are in the head (55 m) (**Figure 2**). The submarine profile is irregular with a pronounced topographic drop from its proximal zone up to its distal area (Araya-Vergara, 1999; Vieira and Simões, 2006). In the proximal area three morainal sills stand out, and other in the fjord mouth, which are forming, between them, several deep basins (Vieira and Simões, 2006; Dowdeswell and Vásquez, 2013).

The bedrock of Europa Fjord comprises rocks from the Southern Patagonian Batholith (SPB) and the Metamorphic Complex of the Eastern Andes (MCEA). The SPB crops out in the central part of the fjord and ice distal areas. On the northern coast, rocks correspond to the oldest set (Jurassic) of the SPB intrusives described by Hervé et al. (2007), while the southern coast includes some of the Jurassic units but it is comprised mostly by Cretaceous granites, granodiorites, and hornblende and biotite tonalites (Sernageomin, 1982). The ice proximal area of the fjord is composed by meta sandstones, phyllites and, to a lesser extent, marbles, cherts, metabasalts and metaconglomerates of the MCEA (Sernageomin, 1982), with ages between Lower Triassic to Upper Devonian (Hervé et al., 2003).

Geophysical Data and Processing

In October-November 2017, CIMAR23 Cruise surveyed several fjords adjacent to SPI to carry out studies on oceanography, biology and sedimentary fjord dynamics, with the science research vessel AGS "Cabo de Hornos." Multibeam bathymetry was obtained using a Kongsberg Simrad EM-122, 12 kHz frequency, whose data were georeferenced with DGPS, and corrected by geostationary satellite. During the cruise, sound velocity profiler (SVP) measurements were made *in situ* to calibrate the depth measurements respect to the sea water velocity of propagation of sound. The bathymetry processing consisted in the manual removal of anomalous beams using the workflow of the CARIS Hips and Sips software. A bathymetric digital grid was generated with a 10 ×10 m resolution, applying an algorithm that uses the "9 × 9 weighted swath angle" method, which aims to create a grid surface based on the intersection angle (CARIS, 2016). Similarly, backscatter data was also processed using the standard CARIS Sips workflow. Geomorphological interpretations were made with the Fledermaus software which allows improved 3D visualization of bathymetric grids. The Fledermaus FMGT module was used to perform a granulometric classification of the seabed sediments according to the program's acoustic library (model), after correcting the data for the angular response of the beams respect to the acoustic strength of the backscatter signal (ARA analysis). Only one superficial sediment sample was obtained in the Europa Fjord during the cruise which was used to verify the ARA analysis. For this sample, standard sieving granulometric analysis was carried out. The sample was classified texturally according to Folk (1974). Other granulometric sediment data served to verify the ARA analysis (Ahumada and Contreras, 1999; Aracena et al., 2011; Boldt et al., 2013). Finally, to build the maps, due to the variability of the acoustic data, the most dominant granulometric classification for specific areas was taken and re-classified texturally.

To improve the bathymetric model of Europa Fjord, we used previously acquired multibeam data from hydrographic cruises carried out by the Hydrographic and Oceanographic Service of the Chilean Navy (SHOA) between 2006 and 2008, which were acquired by the Atlas Fansweep and Hydrosweep MD systems aboard the PSH "Cabrales." These systems use frequencies of 200 and 50 kHz, respectively. The data were corrected by *in-situ* SVP and geo-referenced with real-time DGPS. They were processed in the same way as the data from the AGS "Cabo de Hornos," but the bathymetry was gridded at a resolution of 20 × 20 m. The bathymetric grids obtained from the two vessel data were blended

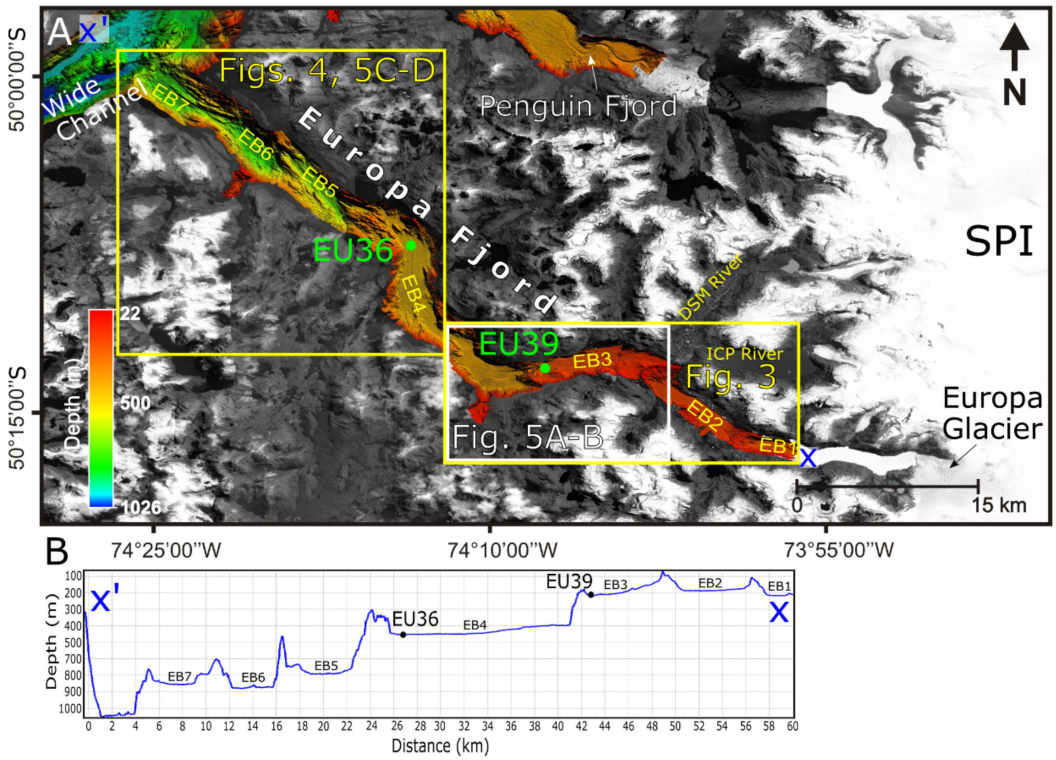

FIGURE 2 | (A) Shaded relief map that shows the coverage of the multibeam bathymetry from Cruise CIMAR 23 and SHOA data. Detailed submarine geomorphology and seafloor sediment distribution are showed in **Figures 3–5**, respectively (boxes). **(B)** Longitudinal bathymetric profile of the Europa Fjord. Europa Basins (EB) are showed.

with GMT software ("grdblend" command) (Wessel et al., 2013; **Figure 2**).

Sub-Bottom Profiler (SBP) data from Kongsberg's CHIRP SBP-120 system aboard the AGS "Cabo de Hornos" could not be obtained in Europa Fjord during CIMAR 23 Cruise. Instead, we used previously acquired SBP data from the NBP0505 Cruise onboard R/V "N.B. Palmer" in 2005 (not used before), which were obtained with a Knudsen 3.5 kHz CHIRP. Visualization of the NBP0505 data was achieved using the system manufacturer's program (Knudsen), adjusting the contrast appropriately (signal amplitude fit). Seismic facies were interpreted according to DaSilva et al. (1997).

Sediment Cores and Analysis

During CIMAR 23 Cruise, two ∼3 m long sediment cores were obtained with a standard gravity corer, in stations EU39 and EU36 (**Figure 2** and **Table 1**). Non-destructive analyses to sediment cores were performed before they were opened and included X-ray Computed Tomography (XT or CT) scanning and magnetic susceptibility measurement of cores. The XT scanning was performed at the Hospital Clinico de la Universidad de Chile (HCUCH) with a Somatom Definition Edge CT Siemens scanner using two X-ray energy levels (dual-energy mode), at 80 and 140 kV, and a spatial resolution that produced volumetric pixels (voxels) of 0.14 mm × 0.14 mm × 0.6 mm. The raw data were processed at HCUCH by a team of medical XT experts, resulting in high resolution and high signal to noise ratio images with cell values of X-rays attenuation in Hounsfield units (HU). Visualization and interpretation of XT processed images was done using the RadiAnt, which allows the 3D and 2D sectional visualization of reconstructed core 3D images. Since at energy values (above 100 kV), X-rays interact with matter mainly through Compton scattering, which is sensitive to the electron density and thus proportional to bulk density, high HU values were interpreted as high density materials. Thus, mapping of high attenuation elements (HAE) of sizes larger than 1 mm throughout the cores was used as a proxy for to the presence of pebbles or large calcareous (fossils?) elements, considering in their identification, the relative contrasting characteristics with the fine sediment matrix. This mapping was done using sectional XT images every 5 cm and manual counting of HAE elements for which HU > 1,400. Bulk magnetic susceptibility measurements (MS) were made using a MS2C Magnetic Susceptibility System

TABLE 1 | Locations of the sediment cores acquired during CIMAR 23 Cruise in 2017.

Core codes	Latitude (S)	Longitude (W)	Depth (m)	Length (m)	Distance from glacier (km)
EU36	50°07′33.6″	74°13′30.36″	447	2.54	20
EU39	50°12′59.54″	74°07′38.17″	222	2.72	13

(Bartington Instruments) which gives an along axis resolution of 2 cm at the Paleomagnetism Laboratory of Universidad de Chile.

Once the corers were opened, a visual description (VD) was performed, and samples were taken for several analyses. Color identification was based on Munsell Color Chart. Laser granulometry was made by a Mastersizer 2000 system, taking samples every 5 cm for each core section (at Geology Laboratory, Universidad de Chile). In addition, samples were taken every 2 cm for the top 30 cm from each core for dating and geochemical analysis. Sedimentation rates were estimated from the radioactive decay of $^{210}Pb_{xs}$ activities in excess (unsupported), considering that the ^{210}Pb flux and the sedimentation rate were constant according to CF-CS model (Goldberg, 1963). Supported activities were estimated from the last constant values (0.99 ± 0.03, 1.52 ± 0.12 dpm g^{-1}) in the range of those values reported by Boldt et al. (2013) in the same area (0.9 ± 0.2 dpm g^{-1}). These activities were assumed to be in equilibrium with ^{226}Ra. The total activities were corrected for the elapsed time between sampling and counting. Sedimentation rates were established from the best exponential fit model (r^2 = 0.82–0.63, p<0.01). Standard deviations (SD) of the ^{210}Pbxs and sedimentation rates estimations were estimated propagating the uncertainties of counting and the deviations of the supported activities estimations (Bevington and Robinson, 1992). Additionally, the activities were modeled according to the CRS model considering the inventories at every 2 cm (Turekian et al., 1980). The ages from both estimations only showed discrepancies in the last two estimations. Finally, to obtain ages at deeper core sections, they were estimated using the software CLAM 3.5.1 (Blaauw, 2010; Rebolledo et al., 2011). The activities were measured at the Chemical Oceanography Laboratory, Universidad de Concepción, using a Canberra QUAD alpha spectrometer, model 7404, obtaining an average error of 0.10 dpm g^{-1}. Geochemical analysis of Organic Carbon, Total Nitrogen, and Nitrogen and Carbon stable isotopes ($\delta^{13}C_{org}$, $\delta^{15}N$) were determined at the Biogeochemistry and Applied Stable Isotopes Laboratory of the Pontificia Universidad Católica de Chile, with an Isotope Ratio Mass Spectrometer (IRMS) Thermo Delta Advantage, coupled to an EA2000 Flash Elemental Analyzer. The associated isotopic error was 0.15 and 0.35 ‰ for Nitrogen and Carbon, respectively. In turn, the associated error in the elemental analysis was 0.002 mg and 0.017 mg for Nitrogen and Carbon, respectively, using a linear regression. The standard used for this calculation was Acetanilide, which contains 71.10% Carbon and 10.36% Nitrogen. For the calculation of the isotopic δ, 4 internal standards previously normalized were used: Acetanilide, Atropine, Caffeine, High Organic Sediment and Glutamic Acid. More methodology details can be found in Rebolledo et al. (2019).

RESULTS

Bathymetry and Geomorphology

The Europa Fjord has a complex seafloor morphology characterized by a series of esplanades or basins identifiable as flat areas separated by oblique or transverse ridges (**Figure 2**). Seven esplanades at different levels of depths are identifiable from SE to NW with: 215, 180, 200, 450, 690, 770, 750 m. Thus, these basins can be named as EB1 to EB7, respectively (**Figures 2–4**). Another basin is also observable outside the fjord in the Wide Channel with a 940 m of depth. Basin EB4 is further divided in two subbasins (EB4-A and EB4-B: **Figures 3**, **4**) based on its morphology. EB4-A has increasing depth toward the fjord's mouth (400–450 m) while EB4-B is mostly a large flat area of ∼450 m; these two sub-basins are connected through a narrow (∼400 m wide) flat bottom channel about 3 km in length. The bottom from EB1 to EB4 is noticeable smoother, flat areas are of lesser extent and more elongated than in basins from EB5 to EB7. The slopes from EB1 to EB7 are < 0.3° interpreted as damming esplanades of sediments (Araya-Vergara, 1997), except for EB3, which has an average slope of ∼1° in the direction of the fjord's mouth, interpreted as an outwash esplanade.

There are two distinct types of shallow areas separating the identified basins: arcuate asymmetrical ridges (AAR) and oblique streamlined sills (OSS). AARs separate EB1 from EB2, EB2 from EB3, and EB3 from EB4 (**Figure 3**), and EB7 from Wide Channel at Europa Fjord's mouth (**Figure 4**), and were interpreted by Dowdeswell and Vásquez (2013) as large moraine ridges generated during stillstand periods within general ice retreat from maximum glacial conditions. OSS define the boundaries between EB4, EB5, EB6 and EB7. They are characterized by streamlined monticules of 10–100s meter in length and irregular morphology and variable extent, often presenting deep narrow channels.

The AAR limiting basin EB1, the most proximal to Europa Glacier (**Figure 3**), has a relief of nearly 100 m and low curvature. It is identified by a series of relatively small ridges on its up-fjord slope (**Figure 3A**) that protrude 5 m from the 4.5° inclined seafloor and are 200, 250, and 400 m of distance from the axis of the main AAR, with the closer ridge (200 m) spatially associated with a long fjord ridge located near the northern coast. The down-fjord (western) side of the AAR has a much steeper slope (11°) and it is characterized by a couple of channels and their tributaries on the deeper part, and by a series of gullies in the upper part.

The AAR separating EB2 from EB3 (74°02′50″ W) has slightly greater relief than the previous one with an elevation difference of ∼115 m (**Figure 3B**) on its up-fjord side. This AAR has greater curvature and an average slope of 3.5° for the up-fjord side and 14° for the down-fjord flank. Small ridges and scour channelizations roughly perpendicular to the crest of the AAR have a relief varying from 5 to 10 m. A few narrow incisions, 300–400 m long and ∼10 m deep, appear near the foothill of the up-fjord flank resembling canyon heads. Gullies are present both sides of the ridge near the top but are more numerous on the down-fjord flank. The top of the AAR is irregular with the central part being deeper than the areas near the coast in both the northern and southern sides, and five depressions 6–10 m deep cut across the ridge.

There are other morphologies in the inner fjord area. On the southern side of the fjord, an underwater extension of the coastal mountain side is observable at ∼110 m depth, but it is flat, and it is surrounded by ridges with a height of ∼20 m respect to inner area. Also, toward the glacier, on the right-most side of the

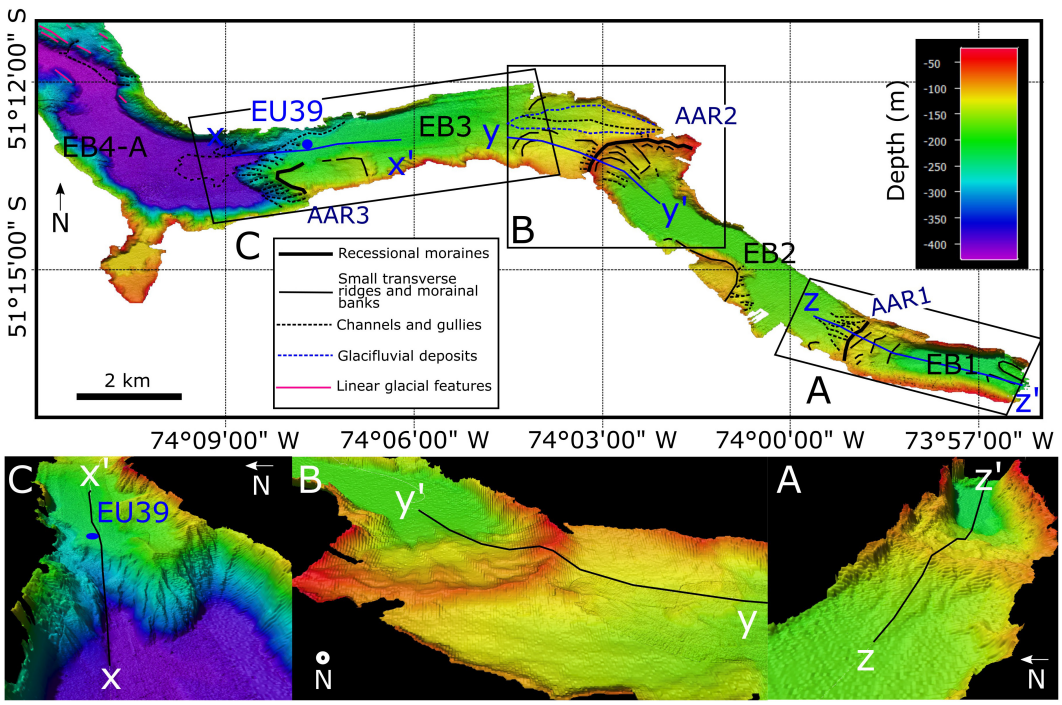

FIGURE 3 | Submarine geomorphology of the inner fjord area from multibeam bathymetry from Cruise CIMAR 23 and SHOA data. Interpretation of landforms are showed. Codes: EB, Europa Basin; AAR, Arcuate Asymmetrical Ridge. **(A)** Moraine proximal subarea and 3D model showing the SBP track for **Figure 6**. **(B)** Moraine medial subarea and 3D model showing the SBP track for **Figure 6**. **(C)** Moraine distal subarea and 3D model showing the SBP track for **Figure 6**, and location of the EU39 sediment core.

Figure 3A, two small arcuate ridges emerge from the flat seafloor on ∼210 m depth.

Basins EB3 and EB4 are separated by a couple of discontinuous and semi-arcuate transverse ridges that are seen only in the southern half of the fjord. The elevation difference between the deeper smooth seafloor of EB3 and the up-fjord areas of EB4 is 170–180 m, with the transition between the two being a cliff area of 15–30°. A large channel dominates the morphology of the northern part of the transition between EB3 and EB4 (**Figure 3C**). The mouth of the channel is 1.3 km wide and 185 m deep and narrows progressively up-fjord, being just 225 m wide at 1.5 km, and 150 m wide and 7 m deep 3 km from the channel mouth. The flanks of the channel have numerous gullies and a smaller side channel on the northern flank, and have steep flanks both sides, with maximum slopes reaching 20–30° in some areas.

The transition between EB4 and EB5 represents the largest depth drop (∼240 m) within Europa fjord, from the distal EB4 seafloor depth of ∼450 m to the proximal EB5 seafloor depth of 690 m (**Figure 4A**). The OSS1 marking the boundary between EB4 and EB5 is flanked by two small esplanades with a depth of ∼420 m located close to both sides of the fjord. The irregular shape of the OSS1 is interrupted by two channels on the down-fjord flank that connect directly to EB5. The OSS1 occurs following an abrupt change in the orientation of the fjord from azimuth 5 to 300°. Two sets of glacial lineations are found on OSS1. The most prominent is characterized by highly elongated monticules like glacial features such as roche moutonnées often observed in deglaciated land areas. These features are 300–1,000 m long and 100–300 m wide and with an azimuth of 310–315°, roughly parallel to the coastline. A smaller set of streamlines features occur partially overlapping or cutting the morphologies of the previous set. This set is characterized by elongated monticules 100–300 m long, mostly symmetrical in the axial direction although a few of them are noticeably asymmetrical, resembling drumlinoid features. Their orientation is ∼15° to the west of the set of larger features and are roughly parallel with the sides of the bottom of the fjord. A third set of streamlines features are observed in this area but east from OSS1 near the coast and are oriented ∼20° oblique to the coastline but roughly parallel to streamlined features observed on land.

The western border of OSS1 falls abruptly down to ∼680 m of depth to the esplanade that conforms EB5 (**Figure 4**). Both EB5 and EB6 are similarly oriented 15–20° oblique to the coastline (EB5 and EB6 azimuth: 330–335°; coastline azimuth: 315–320°), and are separated by OSS2, a 2.5 km long elongated ridge oriented with an azimuth of 335°. Several streamlined features in the area near OSS2 have similar orientation but a set of 300–500 m long elongated monticules overlapping OSS2, are oriented parallel to the coast (azimuth 315–320°). Several drumlinoid features are found in EB6, with some being as small as 150–200 m long and reaching up to ∼500 m in length. They are distributed both at the bottom and the sides of the basin and are spatially accompanied by symmetrical roche moutonnées.

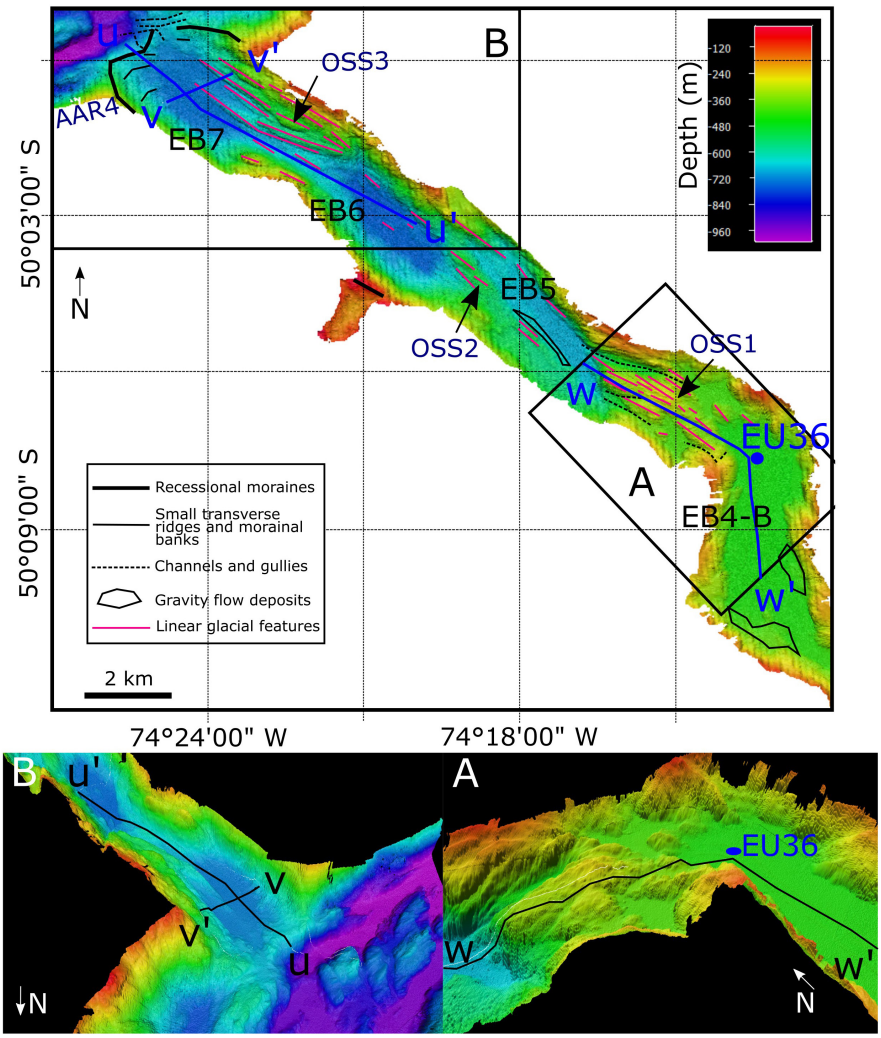

FIGURE 4 | Submarine geomorphology of the outer fjord area from multibeam bathymetry data. Interpretation of landforms are showed. Codes: EB, Europa Basin; AAR, Arcuate Asymmetrical Ridge; OSS, Oblique Streamlined Sills. **(A)** Eastern subarea and 3D model showing the SBP track for **Figure 7**, and location of the EU36 sediment core. **(B)** Western subarea and 3D model showing the SBP tracks for **Figure 7**.

The OSS that forms the transition from EB6 to EB7 (OSS3) has a different morphology than the previous boundary areas (**Figure 4B**). OSS3 is cut by a channel of 3,250 m long and 500 m wide that connects the down-fjord end of EB6 with the up-fjord end of EB7. OSS exhibits prominent 800–2,400 m long elongated features. Notably EB7 is oriented parallel to the southern coastline and is 25–30 m shallower than EB6, which breaks the tendency of down-fjord increasing basin depth. EB7 is characterized by large coastline parallel streamlined features, which reach more than 2–3 km in length and are located only in the northern flank of the fjord. The western limit of EB7 is given by an irregular and arcuate feature 665–685 m deep on its deeper part that marks the mouth of Europa Fjord and the connection to Wide Channel. On its northern part a depression 30 m deep and 700 wide is limited on its northern end by a highly asymmetrical 5 m high monticule perpendicular to the depression. On the up-fjord flank three small ridges form a stepwise morphology with steps occurring roughly every 25 m in depth.

Backscatter and Seafloor Sediments

The type of sediments and their distribution on the seafloor were determined through backscatter data from the AGS "Cabo de Hornos" (no other ship data included in the analysis), so the spatial coverage is less than for the bathymetry mapping. In general, the backscatter data show relatively low values toward the head of the fjord (**Figure 5A**). In EB3, low values of backscatter (< –8 dB) were obtained along the smooth part of the basin while high values are characteristic for AAR3 on its steep down-fjord flank. In EB4 intermediate backscatter values (–25 to –28 dB) predominate on the flat bottom of the basin while higher values are found in the middle of the basin and the narrow channel that connects EB4A and EB4B. High backscatter values dominate EB5, EB6

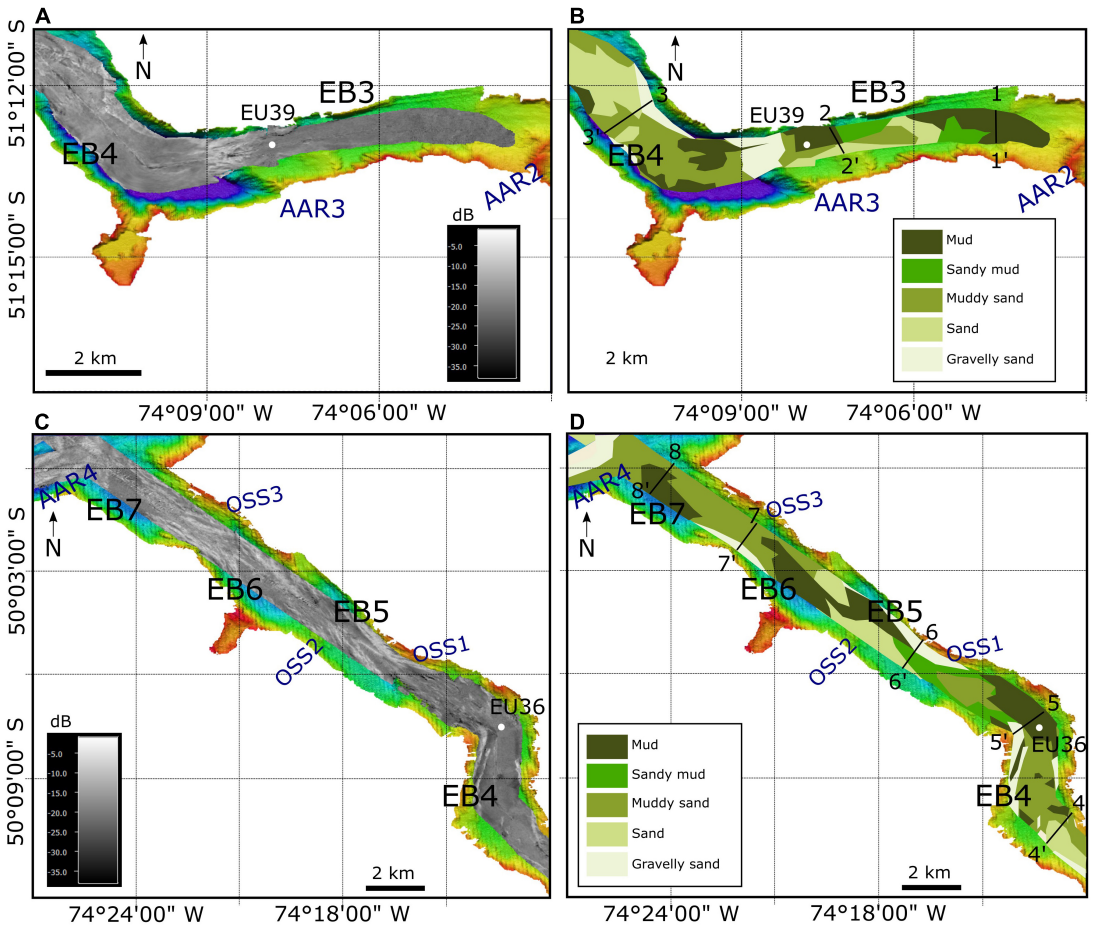

FIGURE 5 | Results from acoustic analysis from Cruise CIMAR 23 multibeam sonar data. **(A)** Backscatter image map for inner fjord area. **(B)** Seafloor sediment textural classification map for inner fjord area. **(C)** Backscatter image map for outer fjord area. **(D)** Seafloor sediment textural classification for outer fjord area. Location of the EU39 and EU36 sediment cores is shown, and example profile locations (e.g., 1–1') for ARA analysis original results are in the **Supplementary Material**.

and EB7 even in the flat parts of these basins. The results of the sediment classification showed that for the inner fjord area, mud is dominant toward the head sector (**Figure 5B**). Coarser material tends to be on the western side of the moraine face, in which its outer slope is composed of sand. For the outer fjord area (**Figure 5C**), intermediate backscatter values predominate, where, for the esplanades, there are low values, and for the structures that border them, higher values, including the moraine located at the fjord mouth. The elongated and pointed shapes of the structures are well defined in the backscatter image. Mud is the main sediment texture for the esplanades, but for that on the eastern side, only its northern part is mud, getting coarser to the south, coinciding in some parts with the identified deposits of gravity flows (sand and gravelly sand) (**Figure 5D**). The same tends to occur in the middle area (around 74°18′W). As was described for the moraine of **Figure 5A**, at the fjord mouth, the moraine is showing coarse material on the outer slope and finer inside. Examples of the original ARA analysis results for the ganulometric classification are available as **Supplementary Material**. The profiles shown in **Figure 5** indicate their position on the map.

Seismic Facies and Stratigraphy

Seismic records are described for the main landforms of the study along profiles shown in **Figures 3**, **4**. **Figure 6A** showed a profile across AAR1 that limits EB1 and EB2 (z'-z profile of **Figure 3A**). The up-fjord flank part of AAR1 showed a series of layers of variable thickness that onlap the acoustic basement and interfinger with layered sub-horizontal seismic facies of EB1. The layers observed in EB1 corresponded to two different seismic facies. Near the bottom and near the top of the sequence, layering was coarse and reflectors limiting them were irregular and discontinuous, while in the middle part of the section subparallel finely spaced reflectors dominated. The bottom facies were distributed filling the rugged acoustic basement resembling ponded sedimentation geometries and forming a smooth flat boundary with the finely layered middle part of the section. The down-fjord flank of AAR1 had a chaotic and coarsely layered seismic character, forming an inclined

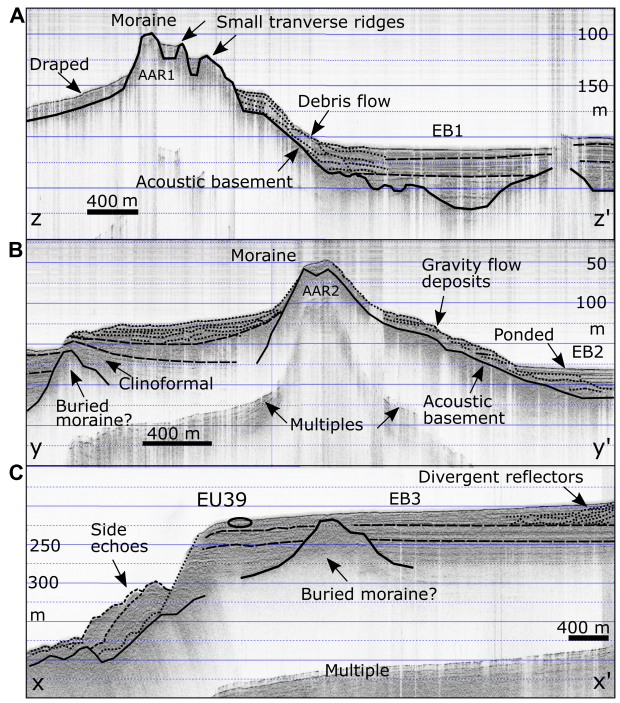

FIGURE 6 | Sub-bottom profile records from cruise NBP0505. Main seismic facies, seismic units (long segmented lines), side-echoes (short segmented lines), acoustic basements (solid lines), and other characters or processes (dotted lines) are showed. **(A)** Proximal subarea for the inner fjord area as showed in **Figure 3A** (z- z'). **(B)** Medial subarea for the inner fjord area as showed in **Figure 3B** (y-y'). **(C)** Distal subarea showed in **Figure 3C** (x-x'). Projected location of the EU39 sediment core is showed.

blanket that onlap onto the acoustic basement. Small transverse ridges appeared at AAR1's top, showing moderate seismic intensity and a chaotic internal reflection character. The third transverse ridge identified by bathymetry truly is a slope change of draped stratified semitransparent seismic facies, interpreted as glacimarine sediment which flow down the slope, forming gravity sediment deposits, who contacts the inner sedimentary basin. This basin showed three main seismic units. The upper had a thin transparent and weak surface layer, and then chaotic with some stratified seismic facies. The middle unit had moderate intensity, parallel ponded and stratified. The lower, was semi-transparent, chaotic and some stratified.

The seismic facies and general architecture of AAR2 are similar to AAR1's. **Figure 6B**, showed a profile across AAR2 (y'-y profile; **Figure 3B**). The up-fjord flank of AAR2 comprised partially chaotic and transparent seismic facies forming layers of irregular thickness that offlap onto each other. The bottom layers underlied sub-horizontal and finely stratified facies of EB2. Other layers of the up-fjord flank interfinger or have a grade with the subhorizontal layers of EB2 which in some cases onlap onto the flank layers. On the down-fjord flank, three main seismic units were present. The top unit had a thin acoustically transparent and forming a mounded seafloor surface. Underlying this unit, chaotic and layered seismic facies were present, with some of the lower ones downlapping onto the bottom unit, while others formed irregularly shaped layers that extend up to a mound that marks the down-fjord extent of the unit. The bottom unit had similar acoustic characteristics, but it thins its layering dips upfjord and is clinoformal with respect to a possible buried moraine due to its seismic facies and the identification of morainal banks nearby detected by the bathymetry.

The seismic section for the western side of EB3 is showed in **Figure 6C** (profile x'-x, **Figure 3C**). The main characteristics of EB3 were its gentle down-fjord slope, the stratified nature of the section, only interrupted by a chaotic or acoustically semi-transparent buried mound, and a series of mounds on the down-fjord end of the section. It was possible to identify three seismic facies that defined three distinguishable seismic units. The top unit was characterized by parallel reflectors that got thin out down-fjord. On the eastern side of the section this unit had several hummocky and subparallel layers that downlap onto the top of the middle unit. The middle unit is characterized by finely spaced layers interbedded with acoustically transparent intervals. The lower unit showed rhythmically layered facies that onlap a mound that extend up to the top of the section but does not crop out on the seafloor.

The seismic architecture of EB4 near the location of core EU36 is shown in **Figure 7A** (profile w'-w; **Figure 4A**). Three seismic units can be recognized in EB4. The top unit, the only one sampled by core EU36, is formed by subhorizontal parallel layers. Underlying the top unit, there was a unit with semi-transparent to chaotic facies and some reflectors of moderate amplitude that hint the presence of layering. The bottom unit had similar seismic facies than the middle one but with lower amplitude, however, layering is discernible. The prominent bathymetric high that forms the boundary between EB4 and EB5, OSS1, is characterized by chaotic and hummocky seismic facies and notable hyperbolic reflectors that indicate the presence of highly reflective or point features. On that bedrock, semi-transparent and hummocky facies are present which can be interpreted as sediment veneer.

The seismic architecture of EB7 is similar to EB4, with three seismic units being recognized in the flat areas of the basin (**Figures 7B,C**, profiles u'-u and v'-v shown in **Figure 4B**). The top unit showed clear layering, but reflectors are of less amplitude than in the top unit of EB4. Underlying the layered top unit, there was chaotic seismic facies with no evident layering that overly bottom facies of layered reflectors and acoustically semi-transparent intervals. The AAR located at the fjord mouth is characterized by high amplitude reflectors with chaotic and hummocky geometries (**Figure 7B**).

Sediment Cores Analysis

Visual Description

Visually, the EU39 core is mainly composed of silt (**Figure 8**). Sedimentary structures such as laminations and lenses were identified. The core can be divided in several visual units according to the general appearance, color and apparent grain size. The Unit 39-A (273–245 cm) composed by silt with mud lenses in smaller proportion than overlying unit, and quartz crystals of ∼ 2 mm size were found. At 74 cm, a rounded

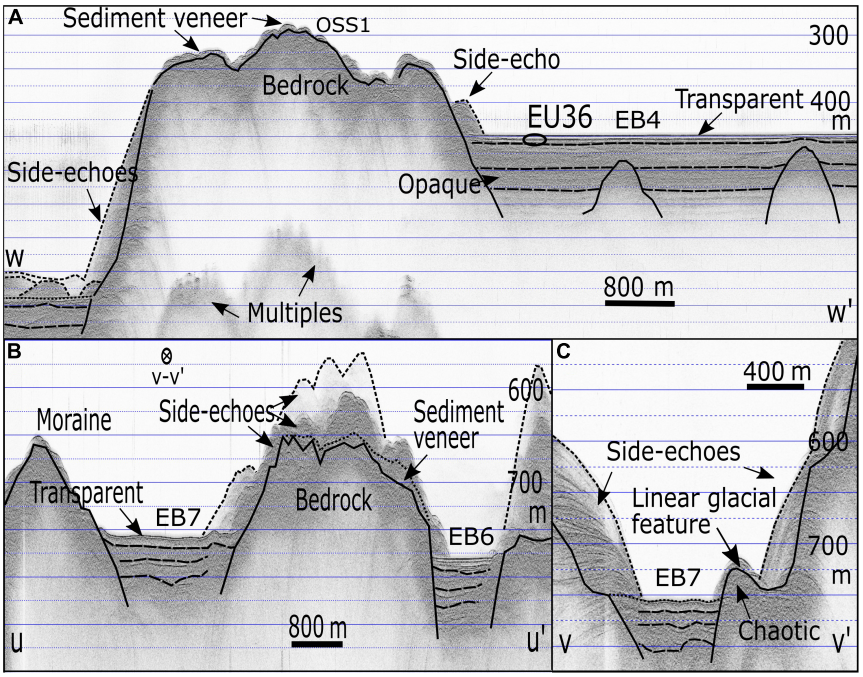

FIGURE 7 | Sub-bottom profile records from cruise NBP0505. Main seismic facies, seismic units (long segmented lines), side-echoes (short segmented lines), acoustic basements (solid lines), and other characters or processes (dotted lines) are showed. **(A)** Eastern subarea of the outer fjord area as showed in **Figure 4A** (w-w'). Projected location of the EU36 sediment core is showed. **(B)** Western subarea of the outer fjord area as showed in **Figure 4B** (u-u'). v-v'track crossing is indicated. **(C)** Crossing of the linear glacial feature and outer basin as showed in **Figure 4B** (v-v').

corneal rock fragment of size ∼1 cm was also found. The color of the unit was dark gray (10YR 4 4/1). The Unit 39-B (247–185 cm) is composed by silt with millimeter-thick mud lenses. Quartz fragments of size ∼ 2 mm were found, and a scaphopod fragment at 13 cm. It presented very thin banded sections of a material with a dark hue. The color of the unit was dark gray (10YR 4 4/1). Unit 39-C (185–143 cm) composed by silty clay, presented mud lens between 160 and 166 cm. Clay color was dark gray (10YR 4 4/1) and mud lens color was gray (10YR 5 5/1). The Unit 39-D (143–60cm) is composed by silty clay with stratifications and millimeter intercalations of fine sediments. At 99 cm there is a branch-like plant remnant no longer than 2 cm. The color of the unit was dark gray (10YR 4 4/1). The Unit 39-E (60–30 cm) is composed by massive silty clay. It presented a small quantity of mud lenses. Normal gradation is recognized in this unit. The color of the unit was gray (10YR 5 5/1). The top of the core (30–15 cm) is composed by massive mud with similar characteristic of the Unit 39-E including color.

Visually, the EU36 core is mainly composed of silt (**Figure 9**). The core can be divided in several visual units. The Unit 36-A (254–116 cm) is composed by massive silt, with a dark gray (5Y 4 4/1) color. The Unit 36-B (101–80 cm), composed by massive silt with a dark gray (5Y 4 4/1) color. This unit presented great loss of interstitial water; the sediment was dry and with low plasticity. The Unit 36-C (80–28 cm) is composed by clayey silt, with periodic intercalations of mud with 2–3 mm thick, and some mud lenses 5–6 mm thick. The color was greenish gray (5 GY 1/5). Unit 36-D (28–13 cm) is composed by massive mud. The section presented a noticeable loss of humidity.

X-Ray Computed Tomography

X-rays attenuation values (Hounsfield Units; HU) obtained through XT scanning allowed us to identify sedimentary structures and intervals of similar attenuation characteristics. Since HU values correlate with the atomic number and the density of the sediments, we used them as one to characterize changes in physical properties of the sediment cores defining XT units as intervals of similar HU values.

XT results for core EU39 are shown in **Figure 8**. Attenuation values vary throughout the core and indicate the existence of intervals of high (900–1,100 HU) and middle-low density materials (750–800 HU)EU39 showed relatively high attenuations at the top and bottom, and between ∼160 to 180 cm depth. The lowest attenuations were found between 245 and 200 cm depth, and between 150 and 158 cm, sections where the abundance of lenses and bioturbation is also greater. Traces of bioturbation were found practically throughout the entire core, this being of variable intensity. Although HAE are variable in quantity, they showed an increasing trend to the core bottom.

The XT results for core EU36 are shown in **Figure 9**. Attenuation values for EU36 also vary throughout the core including intervals of high (HU > 1,100) and low density (700–800 HU). The attenuations of the EU36 core indicate a decrease toward the top, only interrupted by a high attenuation section between 80 and 101 cm depth. We observed signs of intense

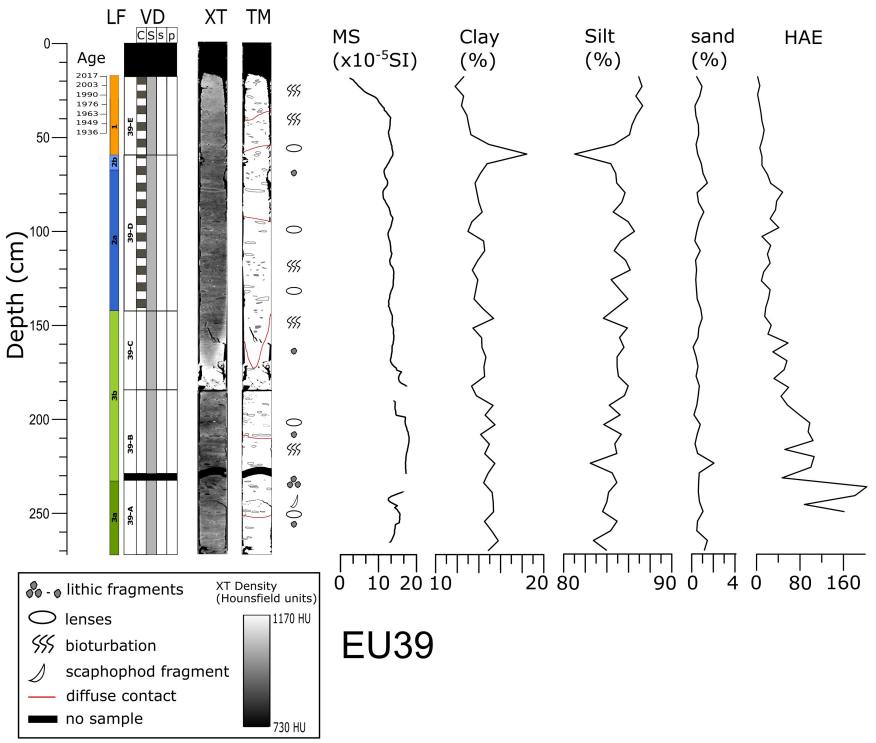

FIGURE 8 | EU39 sediment core with lithofacies identification (LF); Age (from ^{210}Pb dating); original granulometric visual description (VD), showing Clay (C), Silt (S), sand (s) and pebbles (p) contents; X-Ray tomographic image (XT), and interpreted mapping (TM); magnetic susceptibility (MS); laser granulometry showing clay, silt and sand contents; high attenuation elements from XT (HAE).

bioturbation between 146 and 115 cm and in the upper 45 cm of the core. The HAE count is higher in the 50–55 cm section, from which a decreasing trend is observed toward the top. It was not possible to observe HAE from 80 cm toward the bottom of the core.

Laser Granulometry and Magnetic Susceptibility

Laser granulometry and magnetic susceptibility (MS) results for core EU39 are shown in **Figure 8**. There was a slightly increase of MS with depth not exceeding 20 × 10^{-5} SI. Similar pattern is followed by the content of clay and sand, while silt content mirrors clay content and decreases with depth. Average content of clay was ∼15%, for silt ∼84% and for sand ∼1%, which corresponds to silt according to Folk's classification (Folk, 1974).

In core EU36 (**Figure 9**), MS increases with depth (not exceeding 20 × 10^{-5} SI) for the bottom part of the core (> 100 cm), but the top 100 cm shows a broad peak with variable values at the cm to tens of cm scale, indicating relatively high and variable relative proportion of siliciclastic sediments and organic matter, or changes in the quantity or composition of magnetic minerals. Clay and silt content were highly variable in the top 60 cm, while sand content, although variable as well, tended to decrease. Below 60 cm, clay and silt tended to vary around low/high values, respectively, compared with the top 60 cm. Average content of clay was ∼17%, for silt ∼82% and for sand ∼1%, which corresponded to silt according to Folk's classification (Folk, 1974).

Lithofacies

Based on the results from XT scanning, MS, and granulometry, as well as on the visual inspection of cores we defined three main lithofacies (LF1, LF2 and LF3; **Figures 8**, **9**). Lithofacies LF1 corresponded to highly bioturbed and homogeneous mud, including lenses of high and low attenuation (high/low HU values) and a scarce or absent HAE. This lithofacies characterized the top and bottom parts of cores EU39 and EU36. Lithofacies LF2 is composed of bioturbed mud with intercalations of a few millimeter in thickness, some lenses and a variable amount of HAE. Based on differences in the amount of HAE, we distinguished two subfacies: LF2a characterized by increasing amount of HAE with depth; and LF2b, characterized by decreasing amount of HAE with depth. This LF2 lithofacies was distinguished in both cores underlying the top LF1 lithofacies. Lithofacies LF3 is composed by homogeneous and bioturbed mud with the presence of lenses and variable amount of HAE. Like LF2, we defined subfacies LF3a and LF3b based on the relative abundance of HAE being LF3a characterized by noticeable higher presence of HAE relative to LF3b. LF3 was only distinguishable in core EU39.

^{210}Pb Dating and C, N Geochemistry

The ^{210}Pb activities for core EU39 fluctuated between 1.52 and 3.13 dpm g^{-1} and for EU36, between 0.92 and 1.50 dpm g^{-1} (**Figures 10A,G**). The curves lack an exponential decrease with depths, possibly due to the observed bioturbation that

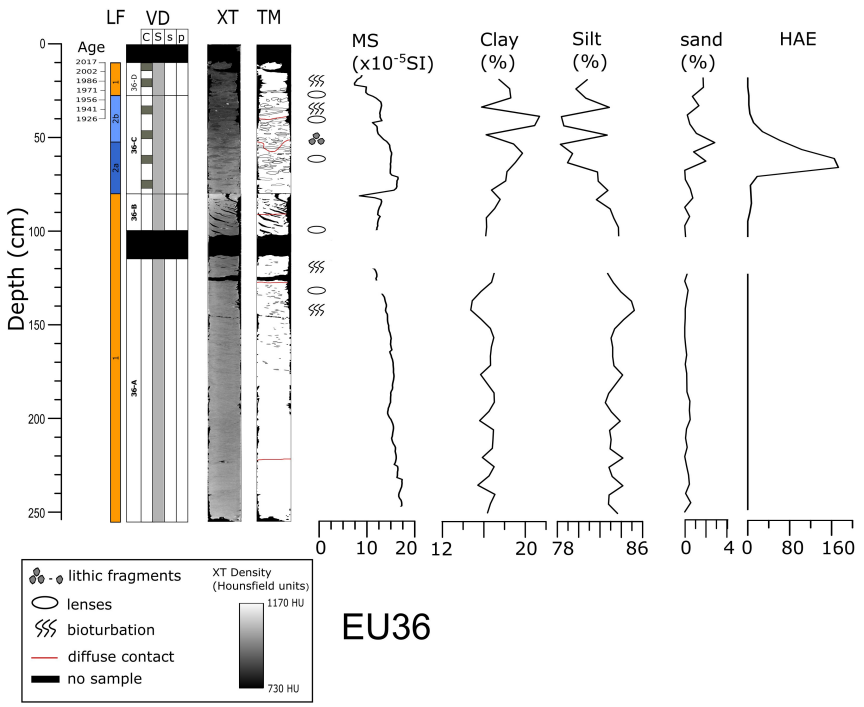

FIGURE 9 | EU36 sediment core with lithofacies identification (LF); Age (from ^{210}Pb dating); original granulometric visual description (VD), showing Clay (C), Silt (S), sand (s) and pebbles (p) contents; X-Ray tomographic image (XT), and interpreted mapping (TM); magnetic susceptibility (MS); laser granulometry showing clay, silt and sand contents; high attenuation elements from XT (HAE).

cause quite homogeneous layers or subsurface higher values on the first 15 cm, related with diffusive and non-local mixing, respectively. The supported activity for EU39 was found to be 1.52 ± 0.12 dpm g^{-1} and 0.97 ± 0.05 dpm g^{-1} for EU36. The sedimentation rates obtained from the best exponential fit model considering the entire core was 0.33 ± 0.05 cm yr^{-1} (r^2 = 0.83, $p < 0.1$) for EU39 and 0.37 ± 0.13 cm yr^{-1} (r^2 = 0.60, $p < 0.01$) for EU36. Estimations below the mixing layer resulted in lower sedimentation rates between 0.08 and 0.09 cm yr^{-1}. The assumption of constant sedimentation rates was based on that the bulk density distribution did not show changes in the depths intervals where ^{210}Pb activities were measured; there were no changes in grain size either, therefore no corrections were made for sediment compaction. The ages obtained with both models, CRS and CF-CS, showed few discrepancies except for the part where the CRS model showed older ages.

Results of C_{org} and N content showed that in each core they vary following the same pattern. A general trend of decreasing C_{org} and N content down-core is observed in core EU39, more prominently for the top ∼20 cm (**Figures 10B,C**). For core EU36 the both content of C_{org} and N were higher and showed greater variability than compared with EU39 (**Figures 10H,I**). The C/N ratio was highly variable throughout the cores (**Figures 10D,J**). In general, the C/N ratios were close to Redfield ratio (7–8), except at the surface in core EU36, reaching higher values (∼9).

The $\delta^{13}C_{org}$ and $\delta^{15}N$ results for EU39 and EU36 are shown in **Figures 10E,F,K,L**, respectively. Generally speaking $\delta^{13}C_{org}$ and $\delta^{15}N$ values were higher for EU36, reaching values close to −23.7‰ for $\delta^{13}C_{org}$ and up to ∼7.5‰ for $\delta^{15}N$. For EU39 both $\delta^{13}C_{org}$ and $\delta^{15}N$ data showed changes at similar depth than the C/N ratio. For EU36, the lower $\delta^{15}N$ data (5−6‰) are consistent with N increases. For EU39, this is observed in the first 5 cm; the increase of N toward recent times corresponded with slight decreases in the isotope but reaching lower values than core EU36. While $\delta^{13}C$ showed low variability in both cores; values were −26‰ for EU39 and ∼24‰ in core EU36, except at surface of this core, decreasing slightly to 25‰.

DISCUSSION

Submarine Landforms and Glacier Retreat

Models show that during the LGM most of the Patagonian fjords including the study area, were covered by glaciers, forming what is referred as the Pleistocene Patagonian Ice Sheet (PPIS) (Davies et al., 2020). In Europa Fjord we found a series of glacial features including glacial lineations, roche mountanee and drumlinoid morphologies indicating that relatively rapid ice flowed along the fjord from the cordillera to the west toward Wide Channel. Some of the features that we describe were recognized by Dowdeswell and Vásquez (2013) for around OSS1 and OSS3, near the middle and the end of the fjord (**Figure 4**). We found that streamlined features are also present in OSS2 and in the area connecting EB4-A and EB4-B, implying that past rapid ice-flow sculpted the sea floor for ∼30 km.

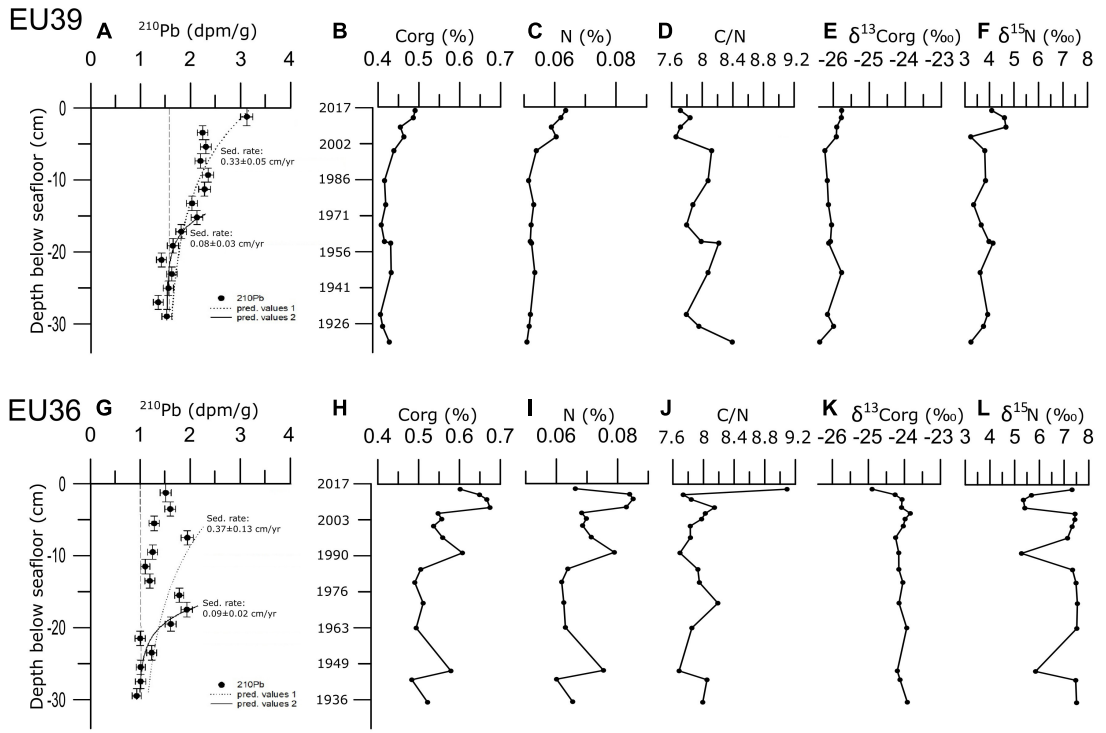

FIGURE 10 | Geochemical variables and sedimentation rates for EU39 **(A–F)** and EU36 **(G–L)** cores, plotted against depth below seafloor (cm) and AD years from 210Pb dating. **(A,G)** ^{210}Pb activity and sediment rates (two models). Vertical segmented lines are showing the supported activity (background). Error bars are indicated (2σ). **(B,H)** Total organic carbon content. **(C,I)** Total nitrogen. **(D,J)** C/N molar. **(E,K)** δ^{13}Corg stable isotope. **(F,L)**δ^{15}N stable isotope.

Evidence that the described streamlined features correspond to sculpted bedrock comes from the high seismic reflectivity, abundant diffraction hyperbolas and hummocky facies found in the seismic record (**Figure 7**). This interpretation is consistent with previous work by DaSilva et al. (1997) and Fernández et al. (2017) that described similar seismic facies in the Patagonian fjords. In some areas, our seismic records suggest that the bedrock is covered by stratified sediment veneers which we interpret as originated from post glacial processes such as hemipelagic sedimentation and mass wasting events. These post-glacial sediment veneers might explain why the backscatter data showed that the seafloor is composed of sediment instead of bare rock for those streamlined feature areas.

Several interpretations about the demise of the PPIS, indicate that rapid ice retreat from Last Glacial Maximum positions occurred probably around 17–15 ka (e.g., Harrison, 2004; McCulloch et al., 2005; Turner et al., 2005; Kilian et al., 2007; Boyd et al., 2008). After the initiation of the deglaciation, a phase of glacier stability occurred around 13.6–12.8 ka (Latest-Pleistocene) in the Magallanes Region, which has been associated with the cooling period registered in Antarctic ice core records known as the Antarctic Cold Reversal (ACR) (e.g., McCulloch et al., 2005; Moreno et al., 2009; García et al., 2012). North of our study area, east of the Northern Patagonia Icefield, a glacial advance occurring ∼11 and 12.8 ka has been associated with the European Younger Dryas (YD) (11–12.8 ka) (Glasser et al., 2012). In the case of the Patagonian fjords, data about the timing and mode of deglaciation is sparse or for some areas like Europa Fjord, non-existing. The few fjords with data are San Rafael Glacier, Gran Campo Nevado and Marinelli Glacier (Kilian et al., 2007; Boyd et al., 2008; Fernández et al., 2012; Bertrand et al., 2017), were radiocarbon dating of glacimarine post-glacial sediments indicate that the Patagonian fjords deglaciated after a period of stability that occurred ∼11 to 13 ka. Therefore, by correlation, we propose that the arcuate mound at the mouth of Europa Fjord, characterized by high amplitude reflectors and diffraction hyperbolas indicating point reflectors and a hard seafloor, represents a fjord-mouth moraine associated to glacier stillstand or readvance coeval with the period of glacier stability ∼11 to 13 ka reported from other areas. This interpretation is supported by the glacial implications of notable difference in depth and width observed at the fjord's mouth area where EB7 shows depths of ∼ 850 mbsl while Wide Channel reaches ∼1,050 mbsl; first, the fjord itself would act as a constriction and pinning point for the ice flowing into Wide Channel as part of the Late Pleistocene Europa Glacier, and second, the wider and deeper Wide channel requires a higher ice flux to maintain grounded flowing ice. It is also consistent with the existence of mouth fjord moraines in other areas of Patagonia (Rodrigo, 1996; Araya-Vergara, 1997, 1999; Vieira and Simões, 2006; Boyd et al., 2008) and other parts of the world (e.g., Shaw, 2016; Munoz and Wellner, 2016). This interpretation is also consistent with the finding

of a depression on the northern part of the Europa Fjord mouth moraine, which porbably represents the incision made by metwater outflow which would have delivered sediment to Wide Channel. In this context, three clearly identifiable bathymetric ridges that run parallel to the main morainal arc, as well as a ridge partially eroded, located 1.35 km up-fjord from the mouth moraine, would represent recessional ridges and moraine associated to the initial of glacier retreat from the outer fjord basins.

The absence of submarine features identifiable as moraines or morainal banks between the fjord mouth moraine until EB4, indicate that ice retreat proceeded rapidly with no stillstands or readvances for quite some time. This interpretation is also consistent with the abundance of streamlined features indicating fast ice flow parallel to the fjord axis. It has been documented from other works in Patagonia that glacial erosion rates scale with glacier retreat rates, which means that in a scenario of general glacier retreat and thinning, the capacity of glacier to sculpt the seafloor would have been enhanced when glaciers were retreating and being confined into the fjords. We note that the absence of land moraines along ∼35 km of fjord is remarkable given the existence of several possible pinning points produced by decreasing depths and constrictions.

The location of AAR2 and AAR3 occur at a major bend of the fjord and coincides with an area of geological contact between Devonian metamorphic rocks and Mesozoic granitoids. We also note that major lineations observed on land seem to continue across the fjord and are manifested in the seafloor as clear linear morphological features. Thus, it is possible that lithological changes and structural heterogeneities along the fjord, influenced the competence and morphology of the bedrock allowing the generation of constrictions that affected the flow of the ancient Europa Glacier, and determined the position of pinning points and moraines. This interpretation is supported by the important influence of morphological changes on glacier dynamics (e.g., Pelto and Warren, 1991; Benn et al., 2007; Barr and Lovell, 2014). We note, however, that AAR3 does not conform with the morphology of typical arcuate moraines such as those described by Dowdeswell and Vásquez (2013). Instead, we recognize two ridges that appear in the bathymetry only in the southern part of the fjord, and that run perpendicular to the fjord near the coast but parallel to the fjord axis near the central part. Our seismic data shows what can be interpreted as either a buried moraine or a subsurface prolongation of the coastal outcrops. It is possible that the origin of AAR3 is mixed, i.e., there was indeed the construction of a moraine at the location of a pinning point or constriction produced by the local bedrock morphology. In this case, the channel in the northern half of the fjord would be there due to the lack of a bedrock obstacle, which allowed the channelization of dense turbiditic flows originated from glacial melt water from Europa Glacier, as well as hyperpycnal fluvial flows from a side valley on the northern coast.

Other remarkable features in the AAR3 area are the high slopes (up to 30°) that limit this feature to the west, the great number of gullies, and the depression at the mouth of the turbidity channel. The origin of the high slopes that limit AAR3 is unclear to us, but we propose two hypotheses. One is that in the past, there was indeed an arcuate moraine built on a bedrock pinning point that was later eroded by flows going through the turbidity channel, and by mass wasting processes related to slope instability. The other possibility is that at some point during the general glacier retreat, a glacier coming from a lateral valley in the southern coast of the fjord, dammed the sediment laden melt waters coming from Europa Glacier resulting in high accumulation of glacial sediments and the formation of a now partially eroded kame terrace.

The arcuate asymmetrical ridge two (AAR2) which limits EB2 and EB3 constitutes a classic example of a submarine moraine. It was first described by Dowdeswell and Vásquez (2013) and interpreted as indicating a period of glacier stability during the overall period of glacier retreat (at the end of the Pleistocene?). We note that AAR2 is located at a major bend in the fjord, 600 m from a fluvial delta formed by rivers Domingo Santa Maria and Ignacio Carrera Pinto that drain two pro-glacial lakes of the same name. The good preservation of AAR2 and the fact that there is no indication of a breach related to fluvial erosion processes, indicates that the moraine is effectively acting as a gabion wall for discharge flows at depths below 70–80 m depth (homopycnal and hyperpycnal flows). We interpret that the channel identified on the seafloor near the northern coast of EB3 was formed by seafloor erosion by dense sediment-laden flows (turbidite flows) from these rivers. In the past, tributary glaciers coming from side valleys joined Europa Glacier and flowed down fjord. It is possible that some of the morphologies observed in EB3, that do not conform to typical cross-fjord arcuate moraine morphologies, where related to the complex glacial retreat history of the area, were side-valley glaciers retreated at a pace different from the main trunk glacier.

Another characteristic of AAR2 is that its flanks showed evidence of repeated gravity flows and slides (**Figure 3B**). On the steeper down fjord flank, facies showing some layering onlapping a curved acoustic basement, resemble the geometries of rotational slides. We noted that the acoustic basement, i.e., the strong seismic reflector below which little acoustic energy could penetrate, is interpreted as a submarine moraine, perhaps at least in part, having a bedrock core as suggested by the apparent continuation of surface bedrock morphologies on the moraine. Furthermore, gullies indicatives of active mass wasting processes are present on both sides of AAR2. On the up-fjord flank large indentations suggest that gullies coalesced to form larger ones whose heads increase the local slope further enhancing the influence of gravity erosional processes. Relatively small and discontinuous ridges on the up-fjord flank could represent the remnant of recessional moraines formed when the ancient Europa glacier started retreating from AAR2.

Closer to the present-day ice front, AAR1 constitutes the most proximal submarine moraine mapped in full so far in Europa Fjord. Both the up-fjord and the down-fjord flanks showed evidence of active mass wasting slope processes with gullies, and channels with steep headwalls, similarly to ARR2. Three small ridges on the up-fjord flank are interpreted as recessional

moraines formed when the glacier retreated from AAR1. We noted that EB1, the most glacier-proximal basin, is 35 m deeper than EB2 which can be interpreted as caused by the younger deglaciation age and consequent thinner sediment fill of the basin. However, it is also possible that the bedrock in EB1 is carved deeper than in EB2, a hypothesis that need future geophysical studies to be solved. On the easternmost area mapped we identified a 12 m high cross fjord asymmetrical feature that might represent another submarine moraine, but we lack seismic data to corroborate it. If so, it would mean that moraines are more closely spaced in the ice proximal basins and imply that glacial variations and associated advance or retreat events of morainal construction (stillstands) are more common for the glacier configuration in which ice is channelized within the fjord and the ice front is relatively close to the present day position, which suggest that the construction of AAR1 and AAR2 is at least in part, related to neoglaciations. Additional efforts to date the glacimarine sediments of EB1 and EB2 are necessary to test this hypothesis.

An important observation is that arcuate submarine moraines only exist at the mouth of Europa fjord and within ∼25 km from the present-day ice front. This suggests that the ice retreated relatively fast or at relatively constant rate, with only short lived stillstands for ∼32 km and from basins ∼750 to 800 m deep to the area of convergence of several ancient glaciers in EB3 which was at the moment ∼250–300 m depth considering a sediment infill of a few tens of meters. Such glacier retreat could be achieved by a sustained negative mass balance that produced a reduction in extent and thickness, which seems possible since the local topography is characterized by low elevations (average ∼200–300 masl for a strip 10 km wide each side from the fjord axis) for about 30 km from the fjord mouth and thus a modest rising of the equilibrium line altitude would have a major impact on the accumulation area.

Glacimarine Sedimentary Processes

From the sediments and seismic analysis, it is suggested that the main processes of sedimentation occurred in a glacimarine environment, whose intensities and properties depended on the glacier front location, the time period and climate variability that influence the retreat/advance velocity and stillstands, among other factors (Domack and McClennen, 1996; Powell and Domack, 2002). In the study area, can be identified the main following processes: subglacial flow, sediment plumes from the ice front and IRD linked by calving. On a second level are: debris flow, slope failure, river or fluviglacial input and non-glacial deposition (biogenic). Oceanographic factors in a glacimarine environment (e.g., Domack and Ishman, 1993) were not analyzed in this work in a direct way, but they could have a role too, considering the tide and wind currents, and turbulence on the moraines (sills) as possible forcing of sediment transport, remobilization and suspension, among others (e.g., Inall and Gillibrand, 2010) and the influence of warmer water masses on tidewater glaciers (e.g., Bendtsen et al., 2017; Holmes et al., 2019).

In general, we identified three main stratigraphic units for the flat seafloor areas characterizing the central part of the successive basins that form Europa Fjord (from EB1 to EB7). The top unit, with an estimated thickness of a few meters up to ∼10 m, showed parallel reflectors and transparent seismic facies, is interpreted as formed by sediments constituted by fine clastic and marine biogenic particles as well as organic matter from land areas. This was the only unit sampled by cores EU36 and EU39, which showed fine granulometry, which explain the internal acoustic transparency observed in the seismic section. In general, the total organic carbon within the top 30 cm is $< 1\%$, although showed an increasing trend from the 15 cm depth to top, which is in good agreement with the decreasing MS near the top of the cores. Similar seismic facies have been associated to ice distal environments (Araya-Vergara, 1997, 1998, 1999; Kilian et al., 2007; Fernández et al., 2017), and have been sampled in other fjords and channels of Patagonia (e.g., DaSilva et al., 1997; Boyd et al., 2008; Fernández et al., 2011; Aracena et al., 2015), where similar sedimentary facies were recognized.

Below the stratigraphic unit with sediment from the water column, seismic facies vary from basin to basin, from stratified facies to opaquer and more chaotic with discontinuous or low amplitude reflectors indicating little variation in acoustic properties (impedance contrast). As indicated before, these facies are found at least a few meters below the seafloor, beyond the reach of our sampling equipment (maximum possible core length was 3 m during the survey). The bottom unit had little internal organization and was mostly characterized by chaotic and semitransparent facies. Similar facies in other Patagonian fjords and channels are interpreted as subglacial till (e.g., DaSilva et al., 1997; Kilian et al., 2007; Boyd et al., 2008; Fernández et al., 2017). Thus, the most likely interpretation of seismic facies is that the bottom unit represents glacial till deposited subglacially, followed by predominantly glacimarine sedimentation represented by the middle unit, with the sequence being topped by stratified post-glacial sediments (e.g., biogenic water column) with glacial (e.g., IRDs) and non-glacial elements (e.g., biogenic, fluvial, mass wasting). The lack of buried moraine ridges suggests that the transition between the successive recessional depositional environments was relatively rapid with no indication of readvance stages.

The complex sedimentary processes taking place in the area are also reflected on the evidence of past and recent mass wasting events and slope erosional processes. The outcropping and buried dipping irregular reflectors and chaotic seismic facies, interpreted as gravity flow deposits in the area (Fernández et al., 2016), are associated with prominent arcuate submarine moraines, and occur on both the up-fjord and the down fjord flanks. This means that they were formed not by direct influence of the ancient Europa glacier but instead by the destabilization of the moraines after ice retreated from them. This interpretation is also supported by the interfingering and lateral transition geometries found in the seismic records and that directly relate several gravity flow units to the bottom and middle units of the respective basin (e.g., see the transition between EB2 and AAR2 in **Figures 6A,B**). On the other hand, sediment derived from fluvial or land mass wasting processes should enter the fjord basins at least at certain locations and be mixed with

marine sediments to form some of the described stratigraphic units. So far, the available data suggest that mass wasting or debris flow input from the coastal areas are not common in the Patagonian Fjords (Boyd et al., 2008; Dowdeswell and Vásquez, 2013; Lastras et al., 2016). An exception are the fjords of northern Patagonia located along the trace of the Liquiñe-Ofqui fault system (e.g., Vargas et al., 2013; Villalobos et al., 2020) where a large landslide related to a Mw 6.2 earthquake on the coastal areas of Aysen Fjord resulted in a major submarine deposit. In that case, the surficial seismic activity was key at generating sufficient energy to trigger the event; in the case of Europa Fjord, there is not known active faulting nor there is records of major surficial earthquakes.

Modern Variability of Glacimarine Sedimentary Processes

The sediments sampled with cores EU36 and EU39 correspond to mud, silt lenses, and variable amounts of lonestones and coarse materials interpreted as ice rafted debris (IRD), which indicate a depositional environment dominated by deposition from suspension processes, bottom flows or currents, and a variable contribution of glacial sediments. The mud and silt lenses are interpreted as the result of the erosion and reworking of bottom sediments either by tidal currents, dense turbiditic flows (hyperpycnal flows) from fluvial systems, or mass wasting processes on steep slope areas. These sedimentary environments and associated processes are well documented in other glacimarine settings such as in Greenland, the Svalbard Region and Antarctica (e.g., Cowan et al., 1997; Ó Cofaigh et al., 2001; Streuff et al., 2017).

Sedimentary processes in the Europa Fjord responded to the distance from glacier front to the deposition site. The passage from a weakly laminated sequence toward a sequence of massive and bioturbed muds, found in both cores, and developed more extensively in the interior of the fjord, is a reflection of the distance from the glacier front, also indicating a lesser influence of turbid plumes for distal areas. The absence of abrupt contacts, inside the cores, would indicate continuity and gradual change of these processes over time, ruling out rapid deposition processes such as turbidity currents on the esplanades where the cores were taken. Geochemical results and organic content in sediments showed the standard distance relation from the ice front, namely, in EU39 (proximal), C_{org}, N, $\delta^{13}C$ and $\delta^{13}N$ are lower than EU36, demonstrating more terrigenous influence from mainly glacimarine processes (Domack and McClennen, 1996; Rebolledo et al., 2011). Additionally, the low organic content at both cores with light $\delta^{13}C$ and $\delta^{15}N$ is also suggesting a higher impact of continental sources when are compared to other marine environments with higher isotopic values in zones of reduced freshwater influence and higher contribution of plankton in the organic sedimentation ($>$ 9; De Pol-Holz, Robinson et al., 2009; Vargas et al., 2011).

Otherwise, the trends observed for MS, in both cores showed an increase of values to older times, reflecting a greater gradual influence of the glacier in the past associated to its sediment yield. On the other hand, the lenses found in the sedimentary records, and the absence of other characteristic of fine-grained turbidite structures, such as erosion contacts, load-bearing structures, ripples, or convolute lamination (Stow and Shanmugam, 1980), allow the idea of the presence of low-energy bottom flows that remobilize surface sediments, especially for EU36 site, but whose energy is not sufficient to form turbidity current properly. Specifically, for EU39 site, there is a flow through channels on the northern part of the fjord, but is still far from it, not influencing this place with more intense energetic processes. Further, the Europa fjord presented much lower sedimentation rates compared to other glacimarine environments associated with temperate glaciers, such as the case of Alaska fjords (Boldt et al., 2013), so this characteristic also indicates low transport, possibly supported by the existence of several large sills that prevent the outwash of sediments and trap them inside individual basins in a ponded pattern (Araya-Vergara, 1997; Fernández et al., 2016), therefore, the sedimentary contributions from the different sources do not add up. Additionally, Europa fjord has lower values of SR compared with other Chilean fjords too (Boyd et al., 2008; Fernández et al., 2011; Boldt et al., 2013) evidencing a lower yield of glacimarine sediments, explained due to larger drainage glacier basin (Aniya et al., 1996) and higher glacier elevation (Fernández et al., 2016), that allows greater accumulation of precipitation.

In general, the values of ^{210}Pb activity are low and have a complex downcore pattern as Boldt et al. (2013) also found for the study area. Low values and same pattern have also been found in other sites of Patagonian fjords (Sepúlveda et al., 2005). The variability in ^{210}Pb activity might be due the effects of stratigraphic disruption produced by bioturbation. Therefore the sedimentation rates would be apparent due to the mixing of particles produce low exponential decay that imply high mass accumulation related with higher sedimentation rates. However, below the most intense mixing layer the values obtained (0.08–0.09 cm yr^{-1}) were in the range of that estimated by Boldt et al. (2013, 0.11 cm yr^{-1}) in one core that had better exponential decay below mixing layer. Other core reported indicated non-steady accumulation rates, probably caused by intense mixing or increased mass accumulation. Thus, the area could have a wider range in the sedimentation depending on the suspended matter loads, that could be underestimated when is only considered the activities below mixing layer. In general, the fjords are zones of higher sedimentation rates characterized by intense deposition of terrigenous material transported from the glaciers fronts being very high close to the glacier front decreasing exponentially toward outer fjord ($>$ 10–0.04 cm yr^{-1}, Zaborska et al., 2006). Our estimations allows establish the recent sedimentation rates in the last 100 years, in the range of the mass accumulation at fjords even if they could be overestimated. The Chilean fjords are dominated by sedimentation of fine-grained particles delivered from turbid meltwater that reach to the seawater from the glacier and glacifluvial systems (Dowdeswell and Vásquez, 2013), in this case, our estimations can account for active landforms that are still being developed today.

Higher percentage of rainfall respect to snow, and temperature-driven surface ice-melt, enhances infiltration of water to the subglacial system promoting sediment outflow through turbid plumes, which would increase the contribution of terrigenous sediments to the fjord system. The positive impact on biogeochemical cycles by the increasing sediment influx to the fjord system (e.g., Seifert et al., 2019), could explain the increase in N since the 1980 decade, found in cores EU36 and EU39. The increase in C_{org} and $\delta^{13}C_{org}$ and $\delta\ ^{15}N$ content for EU39 since the 1980s, is interpreted as due to an increase of influx of terrigenous organic matter from the rivers on the northern coast of the fjord (Ignacio Carrera Pinto and Domingo Santa Maria Rivers). A similar increase in continental organic matter influx since the 1980s was found by Sepúlveda et al. (2005) and Rebolledo et al. (2011) in the fjords of northern Patagonia.

The patterns of C and N variation for the top of core EU36 are more complex and not easily explained by terrestrial influx since the core is in an area with no major rivers nor mountain streams. However, major geochemical changes are also observed since the 1980s which might be partly explained by changes in the distal influx of glacial sediments to the marine environment from iceberg melting. The isotopic changes have been episodic, and the lower $\delta^{15}N$ values resemble the material composition at the core EU39. Notwithstanding, the lower values in $\delta^{15}N$ are concomitant with higher values of Corg and N that would not be related to different $\delta^{13}C$ sources since the profiles were almost constant. These lower values would correspond to the particulate organic matter (POM) and suspended sediment observed in zones influenced by rivers (−25 to −29‰ for ^{13}C, 2–5‰ for ^{15}N; Quiroga et al., 2016), in our case dragged from the glacier, containing organic matter from the continental source.

Regional climate changes over the last decades could also play a role in the isotopes distribution, such as rainfall changes associated to El Niño-Southern Oscillation (ENSO) variability (Ruttland and Fuenzalida, 1991). The Multivariate ENSO Oscillation Index (MEI) of Rebolledo et al. (2011) show fluctuating values for 1900–1940 AD, negative values for 1940–1980 AD, and positive values for the period 1980–2005 AD. The latter period correlates with the recent interval of increasing sedimentation rates and high variability of C and N content. The origin of the variability in C_{org} and N requires further studies, however, we noted that the observed changes are in the multi-annual timescales. We observed though, that the time-scale resolution of our data does not permit to infer the influence of annual or inter annual modes of climate variation. We cannot rule out at least the partial influence of non-climatic nor glacial factors in the variability of the geochemical proxies.

CONCLUSION

Our new high-resolution swath bathymetry and seismic data for Europa Fjord, allowed to improve the understanding of the submarine landforms that characterize the deglaciation of the fjord and subsequent development of sedimentary environments. Seven successive basins, separated by shallow promontories or arcuate submarine moraines, were recognized where sedimentary sequences of tens of meters in thickness exist. Although there is still lack of chronological control to assess the ancient glacial history of the fjord, we demonstrate that:

- The deglaciation of Europa fjord started after a period when the ancient Europa glacier stood still at the mouth fjord where a large arcuate submarine moraine was built. The retreat from the fjord's mouth started slowly as evidenced by recessional ridges on the up-fjord flank of the main moraine, but then proceeded rapidly and/or at constant rate for ∼32 km until the ice terminus grounded at a major fjord bend where several ancient glaciers once converged.
- Prominent submarine arcuate moraines in the inner fjord (∼25 km from present day glacier terminus), indicate that the deglaciation proceeded punctuated by long lived stillstands or periods of glacial advance during a general retreat and thinning stage.
- The coincidence in the location of the inner fjord arcuate moraines with changes in the sinuosity of the fjord, as well as with changes in depth and width, and the location of prominent side glacial valleys, suggest that the location of moraines was partially controlled by morphological factors, such as the existence of "pinning points," or the influence of the ratio between available cross sectional area and ice-flux. The magnitude of the influence of morphological factors on the retreat of other Patagonian Glaciers is a matter of future studies.
- The recognized submarine landforms show evidence of past and currently active erosional and sedimentary processes: slope erosion by mass wasting events (e.g., gullies, channel head-wall erosion, turbidity channels and associated sedimentary lobes). On the flanks of the most proximal arcuate moraines, seismic records show mass wasting deposits extending into the flat basin areas contributing to their sediment infill.

Respect to sedimentary processes acting since the deglaciation of Europa Fjord, we conclude that:

- The stratigraphy of the recognized basins is characterized (from bottom to top) by chaotic or acoustically semi-transparent deposits with or without recognizable layers, followed by several acoustically semi-transparent limited by relatively low amplitude but recognizable reflectors, overlaid by a well stratified units of a few meters to a few tens of meters in thickness. This sequence is characteristic of previously glaciated environments where the bottom units is interpreted as glacial till or diamictite, the middle unit is interpreted as glacimarine, and the stratified unit is interpreted as mostly sediment from water column with glacigenic influence. In case of Europa Fjord, the sequence grades to deposits from mass wasting processes and turbiditic flows, both near the base and near the top.
- Modern sedimentary environments and processes were deduced from two sediment cores (∼3 m long) characterized by highly biologically disturbed mud, fine sediment laminations, silt and mud lenses, and variable amounts of ice rafted debris (IRD). Modern sedimentary

environments are controlled by settling from suspension, deposition by turbid plumes, and calving on the glacier terminus. Lenses show that modern remobilization of sediments is active, probably linked to mass wasting processes.
- Values of ^{210}Pb activity are low and have a complex downcore pattern. From the ^{210}Pb dating, the sedimentation rate determined for the Europa fjord was 0.33 ± 0.05 cm yr^{-1} (EU39), and 0.37 ± 0.13 cm yr^{-1} (EU36), considering highest rates.
- The increase in C_{org} and $\delta^{13}C_{org}$ and $\delta^{15}N$ content for EU39 since the 1980s, indicate a decadal increase in the influx of terrigenous organic matter possibly from the rivers on the northern coast of the fjord. The increase in terrigenous materials is probably linked to the regional increase in temperature and the rainfall/snow ratio indicated by other authors, which should have as direct consequence, an increase in subglacial discharge from melt water and rainfall infiltration. Greater subglacial discharge would imply an increase in glacial sediment outflux with light $\delta^{15}N$.

DATA AVAILABILITY STATEMENT

The original contributions presented in the study are included in the article/**Supplementary Material**, further inquiries can be directed to the corresponding author/s.

AUTHOR CONTRIBUTIONS

CR designed the study, objectives, and fieldwork and wrote the manuscript with the critical contributions of EC and RF. CR, EC, RF, and JA analyzed and interpreted sediment cores. CR and DM processed multibeam bathymetry and backscatter data, which were interpreted by CR and RF. CR processed the seismic data. CR and RF interpreted the seismic data. LR and PM reviewed geochemical data and isotopes results and analyzed the 210Pb dating. All authors contributed to the final version.

FUNDING

This research was funded by CONA grant no. C23 F17-07 of the CIMAR CONA-SHOA Research Program.

ACKNOWLEDGMENTS

We thank the 2017 captain, officers and crew of the AGS "Cabo de Hornos" of the Chilean Navy, and the Hydrographic and Oceanographic Service of the Chilean Navy (SHOA) for the permission of the use of multibeam data obtained by the PSH "Cabrales." We would also like to thank Nicolás Philippi and Stefano Pontarelli for their assistance onboard the CIMAR 23 Cruise, also to Ximena Contardo and Ximena Toledo for field and laboratory management, and the UNAB Facultad de Ingeniería. We are grateful to the reviewers for improving the manuscript giving constructive comments.

SUPPLEMENTARY MATERIAL

The Supplementary Material for this article can be found online at: https://www.frontiersin.org/articles/10.3389/fmars.2022.612021/full#supplementary-material

REFERENCES

Ahumada, R., and Contreras, S. (1999). Contenido de metales (Ba, Cd, Co, Cr, Cu, Ni, Pb, Sr, V y Zn) en sedimentos de los fiordos y canales adyacentes a Campos de Hielo. *Sur. Cienc. Tecnol. Mar.* 22, 47–58.

Aniya, M., Sato, H., Nature, R., Skvarca, P., and Casassa, G. (1996). The use of satellite and airborne imagery to inventory outlet glaciers of the Southern Patagonia Icefield, South America. *Photogramm. Eng. &x Rem. S.* 62, 1361–1369.

Aracena, C., Kilian, R., Lange, C., Bertrand, S., Lamy, F., Arz, H. W., et al. (2015). Holocene variations in productivity associated with changes in glacier activity and freshwater flux in the central basin of the Strait of Magellan. *Palaeogeogr. Palaeoclimatol. Palaeoecol.* 436, 112–122. doi: 10.1016/j.palaeo.2015.06.023

Aracena, C., Lang, C., Iriarte, J., Rebolledo, L., and Pantoja, S. (2011). Latitudinal patterns of export production recorded in surface sediments of the Chilean Patagonian Fjords (41-55°S) as a response to water column productivity. *Cont. Shelf Res.* 31, 340–355. doi: 10.1016/j.csr.2010.08.008

Araya-Vergara, J. (1997). Perfiles geomorfológicos de los fiordos y depresión longitudinal de Norpatagonia. *Cienc. Tecnol. Mar.* 20, 3–22.

Araya-Vergara, J. (1998). El problema genético de los fondos de fiordo Norpatagónicos. *Invest. Mar.* 26, 71–81. doi: 10.4067/S0717-71781998002600007

Araya-Vergara, J. (1999). Perfiles longitudinales de fiordos de Patagonia central. *Cienc. Tecnol. Mar.* 22, 3–29.

Barr, I., and Lovell, H. (2014). A review of topographic controls on moraine distribution. *Geomorphology* 226, 44–64. doi: 10.1016/j.geomorph.2014.07.030

Bendtsen, J., Mortensen, J., Lennert, K., Ehn, J., Boone, W., Galindo, V., et al. (2017). Sea ice breakup and marine melt of a retreating tidewater outlet glacier in northeast Greenland (81°N). *Sci. Rep.* 7:4941. doi: 10.1038/s41598-017-05089-3

Benn, D., Warren, C., and Mottram, R. (2007). Calving processes and the dynamics of calving glaciers. *Earth Sci. Rev* 82, 143–179. doi: 10.1016/j.earscirev.2007.02.002

Bertrand, S., Lange, C., Pantoja, S., Hughen, K., Van Tornhout, E., and Wellner, J. (2017). Postglacial fluctuations of Cordillera Darwin glaciers (southernmost Patagonia) reconstructed from Almirantazgo fjord sediments. *Q. Sci. Rev.* 177, 265–275. doi: 10.1016/j.quascirev.2017.10.029

Bevington, P., and Robinson, K. (Eds) (1992). "Error analysis," in *Data Reduction and Error. Analysis for the Physical Sciences*, (New York, NY: WCB McGraw-Hill), 38–52.

Blaauw, M. (2010). Methods and code for "classical" age-modelling of radiocarbon sequences. *Quat. Geochronol.* 5, 512–518. doi: 10.1016/j.quageo.2010.01.002

Boldt, K., Nittrouer, C., Hallet, B., Koppes, M., Forrest, B., Wellner, J., et al. (2013). Modern rates of glacial sediment accumulation along a 15° S-N transect in fjords from the Antarctic Peninsula to southern Chile. *J. Geophys. Res.* 118, 2072–2088. doi: 10.1002/jgrf.20145

Boyd, B., Anderson, J., Wellner, J., and Fernández, R. (2008). The sedimentary record of glacial retreat, Marinelli Fjord, Patagonia: regional correlations and climate ties. *Mar. Geol.* 255, 165–178. doi: 10.1016/j.margeo.2008.09.001

Briner, J., Bini, A., and Anderson, R. (2009). Rapid early Holocene retreat of a Laurentide outlet glacier through an Arctic fjord. *Nat. Geosci.* 2, 496–499. doi: 10.1038/NGEO556

CARIS (2016). *CARIS HIPS and SIPS 9.1. User Guide*. Phoenix, AR: CARIS.

Carrasco, J., Casassa, G., and Rivera, A. (1998). Climatología actual del Campo de Hielo Sur y posibles cambios por el incremento del efecto invernadero. *Ann. Inst. Patagon. Ser. Cienc. Nat.* 26, 119–128.

Cowan, E., Cai, J., Powell, R., Clark, J., and Pitcher, J. (1997). Temperate glacimarine varves: an example from disenchantment bay, Southern Alaska. *J. Sediment. Res.* 67, 536–549. doi: 10.1306/D42685C7-2B26-11D7-8648000102C1865D

DaSilva, J., Anderson, J., and Stravers, J. (1997). Seismic facies changes a long a nearly continuous 24° latitudinal transect: the fjords of Chile and the northern Antarctic Peninsula. *Mar. Geol.* 143, 103–123. doi: 10.1016/S0025-3227(97)00092-3

Davies, B., Darvill, C., Lovell, H., Bendle, J., Dowdeswell, J., Fabel, D., et al. (2020). The evolution of the Patagonian Ice Sheet from 35 ka to the present day (PATICE). *Earth-Sci. Rev.* 204:103152. doi: 10.1016/j.earscirev.2020.103152

De Pol-Holz, Robinson, R., Hebbeln, D., Sigman, D., and Ulloa, O. (2009). Control son sedimentary nitrogen along the Chilean margin. *Deep Sea Res. II* 56, 1042–1054.

Domack, E., and McClennen, C. (1996). "Accumulation of Glacial Marine Sediments in Fjords of the Antarctic Peninsula and their use as Late Holocene Paleoenvironmental Indicators," in *Foundations for Ecological Research West of the Antarctic Peninsula*, ed. R. M. Ross (Washington DC: American Geophysical Union), 135–154. doi: 10.1029/AR070p0135

Domack, W., and Ishman, S. (1993). Oceanographic and physiographic controls on modern sedimentation within Antarctic fjords. *Geol. Soc. Am. Bull.* 105, 1175–1189.

Dowdeswell, J., Canals, M., Jakobsson, M., Todd, B., Dowdeswell, E., and Hogan, K. (2016). "The variety and distribution of submarine glacial landforms and implications for ice-sheet reconstruction," in *Atlas of Submarine Glacial Landforms: Modern, Quaternary and Ancient*, Vol. 46, eds J. A. Dowdeswell, M. Canals, M. Jakobsson, B. J. Todd, E. K. Dowdeswell, and K. A. Hogan (Burlington House: Geological Society London Memiors), 519–552. doi: 10.1144/M46.183

Dowdeswell, J., and Vásquez, M. (2013). Submarine landforms in the fjords of southern Chile: implications for glacimarine processes and sedimentation in a mild glacier-influenced environment. *Q. Sci. Rev.* 64, 1–19. doi: 10.1016/j.quascirev.2012.12.003

Enderlin, E., and Howat, I. (2013). Submarine melt rate estimates for floating termini of Greenland outlet glaciers (2000–2010). *J. Glaciol.* 59, 67–75. doi: 10.3189/2013JoG12J049

Fernández, R., Anderson, J., Bertrand, S., and Wellner, J. (2012). Gualas Glacier sedimentary record of climate and environmental change, Gold Elefantes, Western Patagonia (46.5°S). *Holocene* 22, 451–463. doi: 10.1177/0959683611425545

Fernández, R., Anderson, J., Wellner, J., and Haller, B. (2011). Timescale dependence of glacial erosion rates: a case study of Marinelli Glacier, Cordillera Darwin, southern Patagonia. *J. Geophys. Res.* 166:F01020. doi: 10.1029/2010JF001685

Fernández, R., Anderson, J., Wellner, J., Minzoni, R., Hallet, B., and Smith, T. (2016). Latitudinal variation in glacial erosion rates from Patagonia and the Antarctic Peninsula (46°S–65°S). *Geol. Soc. Am. Bull.* 128, 1000–1023. doi: 10.1130/B31321

Fernández, R., Gulich, S., Rodrigo, C., Domack, E., and Leventer, A. (2017). Seismic stratigraphy and glacial cycles in the inland passages of the Magallanes Region of Chile, southernmost South America. *Mar. Geol.* 386, 19–31. doi: 10.1016/j.margeo.2017.02.0061

Folk, R. L. (1974). *Petrology of Sedimentary Rocks*. Austin, TX: Hemphill Publishing Company.

García, J., Kaplan, M., Hall, B., Schaefer, J., Vega, M., Schwartz, R., et al. (2012). Glacier expansion in southern Patagonia throughout the Antarctic Cold Reversal. *Geology* 40, 859–862. doi: 10.1130/G33164.1

Gardner, A., Moholdt, G., Graham Cogley, J., Wouters, B., Arendt, A., Wahr, J., et al. (2013). A reconciled estimate of glacier contributions to sea level rise: 2003 to 2009. *Science* 340, 852–857. doi: 10.1126/science.1234532

Glasser, N., Harrison, S., Jansson, K., Anderson, K., and Cowley, A. (2011). Global sea-level contribution from the Patagonian Icefields since the Little Ice Age maximum. *Nat. Geosci.* 4, 303–307. doi: 10.1038/NGEO1122

Glasser, N., Harrison, S., Schnabel, C., Fabel, D., and Jansson, K. (2012). Younger dryas and early Holocene age glacier advances in Patagonia. *Q. Sci. Rev.* 58, 7–17. doi: 10.1016/j.quascirev.2012.10.011

Goldberg, E. D. (1963). "Geochronology with 210Pb, in radioactive dating," in *Radioactive Dating. Proceedings of the Symposium on Radioactive Dating Held by the International Atomic Energy Agency in Co-operation with the Joint Commission on Applied Radioactivity*, (Athens), 121–131.

Harrison, S. (2004). The Pleistocene glaciations of Chile. *Dev. Q. Sci.* 2, 89–103. doi: 10.1016/S1571-0866(04)80115-5

Hervé, F., Fanning, C., and Pankhurst, R. (2003). Detrital zircon age patterns and provenance of the metamorphic complexes of southern Chile. *J. South Am. Earth Sci.* 16, 103–123. doi: 10.1016/S0895-9811(03)00022-1

Hervé, F., Pankhurst, R., Fanning, C., Calderón, M., and Yaxley, G. (2007). The South Patagonian batholith: 150 my of granite magmatism on a plate margin. *Lithos* 97, 373–394. doi: 10.1016/j.lithos.2007.01.007

Holmes, F., Kirchner, N., Kuttenkeuler, J., Krützfeldt, J., and Noormets, R. (2019). Relating ocean temperatures to frontal ablation rates at Svalbard tidewater glaciers: insights from glacier proximal datasets. *Sci. Rep.* 9:9442. doi: 10.1038/s41598-019-45077-3

Inall, M., and Gillibrand, P. (2010). "The physics of mid-latitude fjords: a review," in *Fjord Systems and Archives*, Vol. 344, eds J. A. Howe, W. E. Austin, M. Forwick, and M. Paetzel (London: Geol. Soc. Lond. Spec. Publ), 17–33. doi: 10.1144/SP344.3

IPCC (2014). *Climate Change 2014: Synthesis Report (Fifth Assessment Report of the intergovernmental Panel on Climate Change)*. Available online at: https://archive.ipcc.ch/report/ar5/syr/ (accessed August 27, 2020).

Iriarte, J., Gonzalez, H., and Nahuelhual, L. (2010). Patagonian fjord ecosystems in Southern Chile as a highly vulnerable region: problems and needs. *Ambio* 39, 463–466. doi: 10.1007/s13280-010-0049-9

Kilian, R., Schneider, C., Koch, J., Fesq-Martin, M., Biester, H., Casassa, G., et al. (2007). Palaeoecological constraints on late Glacial and Holocene ice retreat in the Southern Andes (53°S). *Global Planet. Change* 59, 49–66. doi: 10.1016/j.gloplacha.2006.11.034

Koppes, M., Hallet, B., and Anderson, J. (2009). Synchronous acceleration of ice loss and glacial erosion, Glaciar Marinelli, Chilean Tierra del Fuego. *J. Glaciol.* 55, 207–220. doi: 10.3189/002214309788608796

Koppes, M., Hallet, B., Rignot, E., Mouginot, J., Smith Wellner, J., and Boldt, K. (2015). Observerd latitudinal variations in erosion as a function of glacier dynamics. *Nature* 526, 100–103. doi: 10.1038/nature15385

Lastras, G., Amblas, D., Canals, M., and Detsufa Shipboard Party. (2016). "Fjord-flank collapse and associated deformation in Aysén Fjord, Chile," in *Atlas of Submarine Glacial Landforms: Modern, Quaternary and Ancient*, Vol. 46, eds J. A. Dowdeswell, M. Canals, M. Jakobsson, B. J. Todd, E. K. Dowdeswell, and K. A. Hogan (Burlington House: Geological Society London Memiors), 107–108. doi: 10.1144/M46.15

Marzeion, B., Graham Cogley, J., Richter, K., and Parkes, D. (2014). Attribution of global glacier mass loss to anthropogenic and natural causes. *Science* 345, 919–921. doi: 10.1126/science.1254702

Masiokas, M., Rivera, A., Espizua, L., Villalba, R., Delgado, S., and Aravena, J. (2009). Glacier fluctuations in extratropical South America during the past 1000 years. *Palaeogeogr. Palaeoclimatol. Palaeoecol.* 281, 242–268. doi: 10.1016/j.palaeo.2009.08.006

McCulloch, R. D., Bentley, M. J., Tipping, R. M., and Clapperton, C. M. (2005). Evidence for lateglacial ice dammed lakes in the central Strait of Magellan and Bahía Inútil, southernmost South America. *Geogr. Ann. Ser. A Phys. Geogr.* 87, 335–362.

Moon, T., Joughin, I., Smith, B., and Howat, I. (2012). 21st-Century evolution of Greenland outlet glacier velocities. *Science* 336, 576–578. doi: 10.1126/science.1219985

Moreno, P., Kaplan, M., François, J., Villa-Martínez, R., Moy, C., Stern, C., et al. (2009). Renewed glacial activity during the Antarctic cold reversal and persistence of cold conditions until 11.5 ka in southwestern Patagonia. *Geology* 37, 375–387. doi: 10.1130/G25399A.1

Munoz, Y., and Wellner, J. (2016). Local controls on sediment accumulation and distribution in a fjord in the West Antarctic Peninsula: implications for palaeoenvironmental interpretations. *Polar Res.* 35:25284. doi: 10.3402/polar.v35.25284

Ó Cofaigh, C., Dowdeswell, J., and Grobe, H. (2001). Holocene glacimarine sedimentation, inner Scoresby Sund, East Greenland: the influence of fast-flowing ice-sheet outlet glaciers. *Mar. Geol.* 175, 103–129. doi: 10.1016/S0025-3227(01)00117-7

Pelto, M., and Warren, C. (1991). Relationship between tidewater glacier calving velocity and water depth at the calving front. *Ann. Glaciol.* 15, 115–118. doi: 10.3189/S0260305500009617

Pfeffer, W. (2007). A simple mechanism for irreversible tidewater glacier retreat. *J. Geophys. Res.* 112, F03S25. doi: 10.1029/2006JF000590

Post, A., O'Neel, S., Motyka, R., and Streveler, G. (2011). A complex relationship between calving glaciers and climate. *Eos* 93, 305–312. doi: 10.1029/2011EO370001

Powell, R., and Domack, G. (2002). "Modern glaciomarine environments," in *Modern and Past Glacial Environments*, ed. J. Menzies (Woburn, MA: Butterworth-Heinemann), 361–389. doi: 10.1016/B978-0-7506-4226-2.X5000-4

Quiroga, E., Ortiz, P., González-Saldías, R., Reid, B., Tapia, F., Pérez-Santos, I., et al. (2016). Seasonal benthic patterns in a glacial Patagonian fjord: the role of suspended sediment and terrestrial organic matter. *Mar. Ecol. Prog. Ser.* 561, 31–50.

Quiroga, E., Ortiz, P., Reid, B., and Gerdes, D. (2013). Classification of the ecological quality of the Aysen and Baker fjords (Patagonia, Chile) using biotic indices. *Mar. Pollut. Bull.* 68, 117–126. doi: 10.1016/j.marpolbul.2012.11.041

Rebolledo, L., Bertrand, S., Lange, C., Tapia, F., Quiroga, E., Troch, M., et al. (2019). Compositional and biogeochemical variations of sediments across the terrestrial-marine continuum of the Baker-Martínez fjord system (Chile, 48°S). *Prog. Oceanogr.* 174, 89–104. doi: 10.1016/j.pocean.2018.12.004

Rebolledo, L., González, H., Muñoz, P., Iriarte, J., Lange, C., Pantoja, S., et al. (2011). Siliceous productivity changes in Gulf of Ancud sediments (41°S, 72°W), southern Chile, over the last ˜150 years. *Cont. Shelf Res.* 31, 356–365. doi: 10.1016/j.csr.2010.06.015

Rebolledo, L., Sepúlveda, J., Lange, C., Pantoja, S., Bertrand, S., Hughen, K., et al. (2008). Late Holocene marine productivity changes in northern Patagonia-Chile inferred from a multi-proxy analysis of Jacaf channel sediments. *Estuar. Coast. Shelf Sci.* 80, 314–322. doi: 10.1016/j.ecss.2008.08.016

Rignot, E., Rivera, A., and Casassa, G. (2003). Contribution of the Patagonia Ice Fields of South America to sea level rise. *Science* 302, 434–437. doi: 10.1126/science.1087393

Rivera, A., Koppes, M., Bravo, C., and Aravena, C. (2012). Little Ice Age advance and retreat of Glaciar Jorge Montt, Chilean Patagonia. *Clim. Past* 8, 403–4014. doi: 10.5194/cp-8-403-2012

Rodrigo, C. (1996). "Morfología submarina de canales y fiordos: principales morrenas y umbrales. Resultados Crucero CIMAR-Fiordo 1," in *Resúmenes Ampliados CIMAR Fiordo 1*, ed. Comité Oceanográfico Nacional (Valparaíso: SHOA), 11–14.

Ruttland, J., and Fuenzalida, H. (1991). Synoptic aspects of the central chile rainfall variability associated with the southern oscillation. *Int. J. Climatol.* 11, 63–76. doi: 10.1002/joc.3370110105

Sakakibara, D., and Sugiyama, S. (2014). Ice-front variations and speed changes of calving glaciers in the Southern Patagonia Icefield from 1984 to 2011. *J. Geophys. Res* 119, 2541–2554. doi: 10.1002/2014JF003148

Schenk, T., and Csatho, B. (2012). A new methodology for detecting ice sheet surface elevation changes from laser altimetry data. *IEEE Trans. Geosci. Remote Sens.* 50, 3302–3316. doi: 10.1109/TGRS.2011.2182357

Seifert, M., Hoppema, M., Burau, C., Elmer, C., Friedrichs, A., Geuer, J., et al. (2019). Influence of glacial meltwater on summer biogeochemical cycles in Scoresby Sund. *East Greenland. Front. Mar. Sci.* 6:412. doi: 10.3389/fmars.2019.00412

Sepúlveda, J., Pantoja, S., Hughen, K., Lange, C., Gonzalez, F., Muñoz, P., et al. (2005). Fluctuations in export productivity over the last century from sediments of a southern Chilean fjord (44°S). *Estuar. Coast. Shelf Sci.* 65, 87–600. doi: 10.1016/j.ecss.2005.07.005

Sernageomin. (1982). *Mapa Geológico de Chile. Escala 1:1.000.000*. Santiago: Servicio Nacional de Geología y Minería.

Shaw, J. (2016). "Fjord-mouth submarine moraines, SW Newfoundland," in *Atlas of Submarine Glacial Landforms: Modern, Quaternary and Ancient*, Vol. 46, eds J. A. Dowdeswell, M. Canals, M. Jakobsson, B. J. Todd, E. K. Dowdeswell, and K. A. Hogan (Burlington House: Geological Society London Memiors), 79–80. doi: 10.1144/M46.65

Silva, N., Vargas, C., and Prego, R. (2011). Land-ocean distribution of allochthonous organic matter in surface sediments of the Chiloé and Aysén interior seas (Chilean Northern Patagonia). *Cont. Shelf Res.* 31, 330–339. doi: 10.1016/j.csr.2010.09.009

Stow, D., and Shanmugam, G. (1980). Sequence of structures in fine-grained turbidites: comparison of recent deep-sea and ancient flysch sediments. *Sediment. Geol.* 25, 24–42. doi: 10.1016/0037-0738(80)90052-4

Streuff, K., Ó Cofaigh, C., Noormets, R., and Lloyd, J. (2017). Submarine landforms and glacimarine sedimentary processes in Lomfjorden, East Spitsbergen. *Mar. Geol.* 390, 51–71. doi: 10.1016/j.margeo.2017.04.014

Turekian, K., Cochran, K., Benninger, L., and Aller, R. (1980). The sources and sinks of nuclides in Long Island Sound. *Adv. Geophys.* 22, 129–163. doi: 10.1016/s0065-2687(08)60065-5

Turner, K., Forwill, C., McCuloch, R., and Sugden, D. (2005). Deglaciation of the eastern flank of the North Patagonian Icefield and associated continental-scale lake diversions. *Geogr. Ann. A* 87, 363–374. doi: 10.1111/j.0435-3676.2005.00263.x

Vargas, C., Martínez, R., San Martin, V., Aguayo, M., Silva, N., and Torres, R. (2011). Allochthonous subsidies of organic matter across a lake–river–fjord landscape in the Chilean Patagonia: implications for marine zooplankton in inner fjord áreas. *Cont. Shelf Res.* 31, 187–201. doi: 10.1016/j.csr.2010.06.016

Vargas, G., Rebolledo, S., Sepúlveda, S. A., Lahsen, A., Thiele, R., Townley, B., et al. (2013). Submarine earthquake rupture, active faulting and volcanism along the major Liquiñe-Ofqui Fault Zone and implications for seismic hazard assessment in the Patagonian Andes. *Andean Geol.* 40, 141–171. doi: 10.5027/andgeoV40n1-a07

Vieira, R., and Simões, J. (2006). Coast of fjords in Central Patagonia, Chile, submarine morphology and acoustic facies. *Rev. Bras. Geof.* 24, 5–24. doi: 10.1590/S0102-261X2006000100001

Villalobos, A., Easton, G., Maksymowicz, A., Ruiz, S., Lastras, G., De Pascale, G. P., et al. (2020). Active faulting, submarine surface rupture, and seismic migration along the Liquiñe-Ofqui Fault System, Patagonian Andes. *J. Geophys. Res.* 125:e2020JB019946. doi: 10.1029/2020JB019946

Wessel, P., Smith, W., Scharroo, R., and Wobbe, F. (2013). Generic mapping tools: improved version released. *Eos* 94, 409–410. doi: 10.1002/2013EO450001

Zaborska, A., Pempkowiak, J., and Papucci, C. (2006). Some sediment characteristics and sedimentation rates in an Acrtic Fjord. *Ann. Environ. Prot.* 8, 79–96.

Conflict of Interest: The authors declare that the research was conducted in the absence of any commercial or financial relationships that could be construed as a potential conflict of interest.